



HAL
open science

Successive Strong Electrostatic Adsorptions of [RhCl₆]³⁻ on Tungstated-Ceria as an Original Approach to Preserve Rh Clusters From Sintering Under High-Temperature Reduction

Jeffrey Miller, Neil Schweitzer, Mimoun Aouine, Philippe Vernoux, Abdelmalik Boufar, Juliette Blanchard, Jean-Marc Krafft, Christophe Méthivier, Céline Sayag, Frédéric Ser, et al.

► To cite this version:

Jeffrey Miller, Neil Schweitzer, Mimoun Aouine, Philippe Vernoux, Abdelmalik Boufar, et al.. Successive Strong Electrostatic Adsorptions of [RhCl₆]³⁻ on Tungstated-Ceria as an Original Approach to Preserve Rh Clusters From Sintering Under High-Temperature Reduction. *Journal of Physical Chemistry C*, 2021, 125 (45), pp.25094-25111. 10.1021/acs.jpcc.1c07644 . hal-03449235

HAL Id: hal-03449235

<https://hal.science/hal-03449235v1>

Submitted on 25 Nov 2021

HAL is a multi-disciplinary open access archive for the deposit and dissemination of scientific research documents, whether they are published or not. The documents may come from teaching and research institutions in France or abroad, or from public or private research centers.

L'archive ouverte pluridisciplinaire **HAL**, est destinée au dépôt et à la diffusion de documents scientifiques de niveau recherche, publiés ou non, émanant des établissements d'enseignement et de recherche français ou étrangers, des laboratoires publics ou privés.

Successive Strong Electrostatic Adsorptions of $[\text{RhCl}_6]^{3-}$ on Tungstated-Ceria as an Original Approach to Preserve Rh Clusters From Sintering Under High-Temperature Reduction

Jeffrey T. Miller,¹ Neil M. Schweitzer,² Mimoun Aouine,³ Philippe Vernoux,⁴ Abdelmalik Boufar,⁵ Juliette Blanchard,⁵ Jean-Marc Krafft,⁵ Christophe Méthivier,⁵ Céline Sayag,⁵ Frédéric Ser,⁶ Mickaël Sicard,⁶ Cyril Thomas^{5,*}

1- Purdue University, Davidson School of Chemical Engineering, 480 Stadium Mall Drive, West Lafayette, IN 47907-2100, USA

2- Department of Chemical and Biological Engineering, Northwestern University, Evanston, Illinois 60208-3113, USA

3- Univ Lyon, Université Claude Bernard Lyon 1, CNRS, Institut Lumière Matière, F-69622 Villeurbanne, France.

4- Univ Lyon, CNRS, Université Claude Bernard Lyon, IRCELYON, 2 Av. Albert Einstein, F-69626 Villeurbanne, France.

5- Sorbonne Université, CNRS, Laboratoire Réactivité de Surface, LRS, F-75005 Paris, France

6- Multi-Physics for Energetics Department, ONERA Université Paris Saclay, F-91123, Palaiseau, France.

* To whom correspondence should be addressed:

Dr. Cyril Thomas

Sorbonne Université, CNRS, Laboratoire Réactivité de Surface, LRS, UMR CNRS 7197, 4 Place Jussieu, Tour 43-53, 3^{ème} étage, Case 178, F-75252, Paris, France

e-mail: cyril.thomas@sorbonne-universite.fr

Tel: + 33 1 44 27 36 30

Fax: + 33 1 44 27 60 33

ABSTRACT:

Supported transition metal materials have been identified as ideal candidates for decades to catalyze various reactions of interest in the fields of hydrocarbon refining, energy and environmental catalysis. As the resources in transition metals on earth are known to be limited, it appears to be of the utmost interest to improve the efficiency of the catalytic materials in achieving the best use of these transition metals, in other words the highest metal accessibility when supported on oxide carriers. The present study demonstrates that the deposition of oxotungstates (with a W surface density of 1.3 W/nm^2) coupled with the selective deposition of Rh on the CeO_2 surface (via successive strong electrostatic adsorptions of an anionic $[\text{RhCl}_6]^{3-}$ precursor) significantly reduces Rh sintering after reduction at $600 \text{ }^\circ\text{C}$ under H_2 compared to a W-free CeO_2 support. Oxotungstates are found to decrease the number of nucleation sites of CeO_2 and, therefore, to act as spacers leading to the isolation of the nucleation sites. Oxotungstates may also act as a physical barrier preventing the sintering of the Rh metallic phase in the course of the reduction step at high temperature. Various morphologies of subnanometric Rh clusters exhibiting a limited atomicity (4 to 13 Rh atoms) were considered and most were found to be consistent with the very low coordination numbers of 4.0 ± 0.2 determined experimentally by EXAFS. The coordination numbers and the H_2 chemisorption data led the conclusion that the Rh subnanometric clusters must be at the maximum two to three Rh layers thick and not larger than 5 Rh atoms. The benzene hydrogenation turnover frequencies at $50 \text{ }^\circ\text{C}$ were found to be similar on both the subnanometric Rh clusters and the 2.5 nm Rh nanoparticles ($0.12 \pm 0.3 \text{ s}^{-1}$).

1. INTRODUCTION

Supported transition metal materials have been identified as ideal candidates for decades to catalyze various reactions of interest in the fields of hydrocarbon refining, energy and environmental catalysis. As the resources in transition metals on earth are known to be limited, it appears to be of the utmost interest to improve the efficiency of the catalytic materials in achieving the best use of these transition metals, in other words the highest dispersion (metal accessibility) of the metals when supported on oxide carriers. Many studies have been devoted to the preparation of highly-dispersed supported metal catalysts¹⁻³ resulting in the formation of nanoparticles of the smallest size in order to ensure the highest accessibility of the metal used. Recently, this goal led to the preparation of the so-called single atom catalysts,^{2, 4-12} for which it is assumed that the metals deposited are fully accessible for the catalytic reactions of interest because of being present as atomically dispersed, thus achieving the greatest rational use of these metals. Yet preparing supported atomically-dispersed transition metals is far from being trivial^{4, 8, 13, 14} and the deposition of transition metals on oxide carriers not only results in highly-dispersed species but also most often in the formation of nanoparticles of various morphologies essentially as spherical or cuboctahedron three-dimensional (3D) clusters,^{1, 2, 15} whose sizes are in general rather difficult to precisely control. In several literature reports, the morphology of noble metal particles was also ascribed as rafts (2D structures)^{10, 11, 16-18} and it has been shown that such a peculiar morphology could result from the transformation of nanoparticles at higher reduction temperatures.¹⁹ For 3D nanoparticles, the accessibility of the metal atoms, in other words the ratio of the metal surface atoms to that of the total number of metal atoms in the sample (also defined as the metal dispersion²⁰), increases as the size of the nanoparticles decreases. The dispersion of particularly costly transition metals, such as those from Platinum Group Metals, has been found of the utmost interest in the field of emission control^{21, 22} and

ceria-related materials have been shown to be instrumental to preserve their dispersion under rather severe operating conditions.^{23, 24}

Various methods have been used to deposit transition metals on oxide carriers. Among these methods, the deposition of transition metals by strong electrostatic adsorption (SEA)³ has been found to lead to highly-dispersed Pt on oxides.²⁵ This method aims at favoring the interaction of the positively/negatively-charged metal complexes with oxide surfaces whose negative/positive charge can be tuned finely by setting the pH of the adsorption medium above/below the point of zero charge (PZC) of the corresponding oxides,²⁶⁻²⁸ respectively. Although SEA has been used commonly for the deposition of transition metals on various single oxides,³ the attempts to deposit selectively a particular metal on a more complex oxide, namely an oxide supported on another oxide with both of these oxides exhibiting significantly different PZCs, are scarce. Among these studies, Regalbuto and co-workers selectively deposited $[\text{MnO}_4]^-$ anions on Co_3O_4 supported on TiO_2 .²⁹ The intimate contact between the Mn and Co species was found to result in an increase in light olefins, C_{5+} selectivity and chain growth probability for the Fischer-Tropsch synthesis. Later, Regalbuto and co-workers also used the SEA process to provide insights into the deposition of Pt on amorphous silica-aluminas³⁰ and into the proximity of hydrogenation and acid sites needed for the bifunctional transformation of *n*-heptane.³¹ By controlling the deposition of Pt either on the alumina binder or into the Y zeolite, Martens and co-workers showed that the closest proximity between the metal and acid sites of a catalyst appeared to be surprisingly detrimental for bifunctional reactions.³² A modification in the selectivity of the *n*-heptane hydrocracking reaction was also reported by Ben Moussa et al. depending on the location of the Pt^0 nanoparticles either on beta zeolite or alumina, and on the intimacy of these latter oxide phases.³³ More recently, Christopher and co-workers demonstrated that the one-step selective deposition of a positively-charged Rh precursor ($[(\text{H}_2\text{NCH}_2\text{CH}_2\text{NH}_2)_3\text{Rh}]^{3+}$) near negatively-charged ReO_x species supported on

Al₂O₃ led to highly-dispersed promisingly active Rh species for the hydroformylation of ethylene.³⁴

An earlier work showed that the deposition of about 1.2 wt% Rh via incipient wetness impregnation on tungstated ceria-zirconia supports did not occur selectively on one particular oxide.³⁵ One reason for this could be that both oxides were positively charged at the pH of the Rh aqueous solution, which did not favor any preferential interaction of the positively-charged [Rh(H₂O)₆]³⁺ complex with only one oxide. In addition, it was found that the hydrogenating properties of the prepared samples decreased as the W density increased, because the Rh species interacting with the tungstate phase were found to be much less active compared to those interacting with ceria-zirconia.

CeO₂-related materials have been found to exhibit properties that allowed the preservation of highly-dispersed metal species, in particular for noble metals for which the greatest accessibility should be sought due to their elevated cost and limited availability. Apart from several studies in which high temperature treatments were demonstrated to be instrumental for the stabilization of atomically-dispersed metal species,^{4, 8} the deposition of Rh on CeO₂-related materials generally leads to the formation of Rh nanoparticles of about 2-4 nm³⁶⁻³⁹ for which the atom accessibility can be estimated to be less than about 55 %. Apart from the automotive emission control field in which noble metals, including Rh, supported on ceria-related oxides have demonstrated their unique capability for decades,²¹⁻²³ Rh-CeO₂ has been shown rather recently to be a promising catalyst for ethanol reforming reactions.⁴⁰⁻⁴²

The present study was aimed at preparing Rh clusters highly dispersed on a ceria support modified by tungstates in order to preserve these clusters from sintering after high-temperature reduction. As ceria and WO₃ exhibit rather different PZCs,^{26, 27} the present study shows that the SEA method could be used to deposit Rh from the [RhCl₆]³⁻ complex selectively on the ceria phase, by setting the pH of the aqueous adsorption solution to a value intermediate to those of

the PZCs of CeO₂ and WO₃. Yet it was found that the presence of tungstates drastically limited the amount of Rh that could be deposited on the tungstated-ceria material by a single SEA process so that the selective adsorption process needed to be repeated successively to increase the Rh loading of the samples. This series of samples, together with reference samples obtained on the tungstate-free CeO₂ pristine support, were thoroughly characterized by XRF, N₂ sorption, Raman, XAS, XPS, NO_x-TPD, N₂-FTIR, low-temperature H₂ chemisorption, ETEM and eventually investigated in the benzene hydrogenation catalytic model reaction. Interestingly when the amount of Rh was increased by a factor of about five, namely from about 0.2 to about 0.9 wt%, the size of the Rh clusters remained essentially constant and subnanometric, whereas the hydrogenating properties normalized per g of Rh in the sample were found to increase by a factor of about 2 as the Rh loading increased. Rh clusters of various morphologies are discussed to account for the apparently conflicting experimental data recorded on such peculiar samples.

2. EXPERIMENTAL SECTION

2.1. Materials

The CeO₂ support (HSA5, Solvay) was firstly calcined at 750 °C (2 °C/min) for 4 h. This resulted in a significant decrease in its specific surface area (from more than 200 m²/g in the non calcined state to about 70 m²/g after calcination at 750 °C) and the suppression of its microporosity. As in our earlier studies,^{35,43} W was then deposited on ceria by incipient wetness impregnation with aqueous solutions of (NH₄)₆H₂W₁₂O₄₀ (Aldrich) leading to various W loadings up 15.4 wt%, which corresponds at maximum to a W surface density³⁵ of 7.8 W/nm²_{CeO₂}. After aging at RT for 6 h and drying at 100 °C overnight, the tungstated materials were calcined in air at 500 °C (2 °C/min) for 2 h in a muffle furnace. The prepared supports

will be denoted as $W(W/\text{nm}^2_{\text{CeO}_2})\text{-CeO}_2$ where $W/\text{nm}^2_{\text{CeO}_2}$ refers to as the W atomic surface density. Rh was introduced on $W(1.3)\text{-CeO}_2$ via successive strong electrostatic adsorptions (SEAs). 12 g of $W(1.3)\text{-CeO}_2$ were firstly contacted with 50 mL of a 15.5×10^{-3} mol/L aqueous solution of ammonium hexachlororhodate hydrate ($\text{Rh}(\text{Cl}_6)(\text{NH}_4)_3 \cdot \text{H}_2\text{O}$, STREM Chemicals). The pH of the resulting suspension was then set to 4 with the addition of HNO_3 and/or NH_4OH . The suspension was stirred vigorously for 2 h. The solid was centrifuged (9,000 rpm) and washed once with distilled water (50 mL) before being centrifuged once again. The solid was then dried overnight at 100 °C and calcined at 400 °C (2 °C/min) for 2 h. This calcination temperature was selected on the basis of the earlier work of Varga et al. in which it was shown that such a temperature was sufficient to decompose RhCl_3 on CeO_2 .³⁸ 2 g of the calcined solid were kept apart, denoted as $\text{Rh}/W(1.3)\text{-SEA}_1$ indicating that this sample was obtained after the first SEA experiment. The remaining $\text{Rh}/W(1.3)\text{-SEA}_1$ solid (about 10 g) was contacted with the ammonium hexachlororhodate solution preserved after the first SEA experiment and submitted to the same protocol as that described previously for $\text{Rh}/W(1.3)\text{-SEA}_1$. SEA experiments were thus carried out successively up to 5 times and the corresponding samples will be denoted as $\text{Rh}/W(1.3)\text{-SEA}_i$ (where i refers to as the number of successive SEA performed on the sample). Using this methodology, about 92 % of the Rh introduced initially in the solution was found to be deposited on the series of samples.

Rh was also deposited on pure CeO_2 ($W(0.0)\text{-CeO}_2$) in the conditions of the SEA using $\text{Rh}(\text{Cl}_6)(\text{NH}_4)_3$ (3 g of CeO_2 contacted with 51.3 mL of a 5.4×10^{-3} mol/L aqueous solution of ammonium hexachlororhodate hydrate) and $\text{Rh}(\text{H}_2\text{O})_6(\text{NO}_3)_3$ (Aldrich). These samples will be denoted as $\text{Rh}_{\text{Cl}}/W(0.0)\text{-CeO}_2$ and $\text{Rh}_{\text{NO}_3}/W(0.0)\text{-CeO}_2$.

2.2. Characterization

Chemical analysis of the supported catalysts was performed by X-ray Fluorescence using a XEPHOS He III (AMETEK) spectrometer.

N₂-sorption measurements were carried out on a Belsorp max instrument (Bel Japan) at 77 K. Prior to the sorption experiments, the samples were outgassed for 3 h at 300 °C. Specific surface area was determined using the BET equation in the range $0.1 > P/P_0 > 0.4$.

Raman spectra of the samples were collected from a KAISER (RXN1) Optical system equipped with a charge-coupled detector (CCD) and a laser with $\lambda = 785$ nm (power, 5 mW; resolution, 4 cm⁻¹; accumulation time, 10 s; 30 scans per spectrum). A microscope with an X50 long working distance (W.D. = 8.0 mm) lens was used.

Transmission X-ray absorption spectroscopy (XAS) of the Rh-K (23.220 keV) and W-L₃ (10.207 keV) edges of the in situ reduced Rh/W(1.3)-SEAi series and Rh_{NO3}/W(0.0)-CeO₂ were measured at Argonne national Laboratory's (Argonne, IL) Advanced Photon Source (APS) on the Materials Research Collaborative Access Team's (MRCAT) bending magnet beamline in sector 10-BM. Catalysts samples were pressed into an in situ cell and reduced at 600 °C in 4% H₂ prior to measurements at room temperature. Spectra of Rh and W foils were collected along with the samples for energy calibration. The data fitting was done with the software WinXAS 97, version 3.0. A Rh foil was used as a reference for both XANES and EXAFS fitting (N Rh-Rh = 12, R = 2.69 Å). WO₃ and Na₂WO₄ (N W-O at 1.78 Å) were also used as W references. The Rh EXAFS were fit in R-space from $\Delta k = 2.8-11.4$ Å⁻¹ and $\Delta R = 1.3 - 2.8$ Å, and W EXAFS was fit from $\Delta k = 2.6-11.3$ Å⁻¹ and $\Delta R = 0.9 - 1.7$ Å.

XP spectra were collected on an Omicron Scienta (Argus) X-ray photoelectron spectrometer using a monochromated Al K α (h ν = 1486.6 eV) radiation source having a 300 W electron beam power. Charge compensation was carried out using an electron beam having an energy of 1 eV and an emission current of 10 mA. The emission of photoelectrons from the

sample was analyzed at a takeoff angle of 45° under ultrahigh vacuum conditions (1×10^{-8} Pa). XP spectra were collected at pass energy of 20 eV for C 1s, O 1s, W 4f, Ce 3d, Ce 4d, and Rh 3d core XPS levels. After data collection, because of the known difficulties in referencing the binding energies to the C1s line,⁴⁴ the binding energies were calibrated with respect to the binding energy of the O 1s peak at 529 eV.^{45,46} All of the binding energies reported in this work were measured within an accuracy of ± 0.2 eV. The peak areas were determined after subtraction of a Shirley background. The atomic ratio calculations were performed after normalization using Scofield factors.⁴⁷ Spectrum processing was carried out using the Casa XPS software package and Origin 7.1 (Origin Lab Corporation). The Rh(wt%)/W(1.3)-SEA_i series was analyzed after ex situ reduction at 600 °C for 2 h and careful exposure to ambient atmosphere at RT prior to introduction in the XPS device. Some of the samples (Rh/W(1.3)-SEA₂, Rh/W(1.3)-SEA₃, Rh/W(1.3)-SEA₅ and Rh_{Cl}/W(0.0)-CeO₂) were also analyzed in their oxidized form (after ex situ calcination at 400 °C) and after in situ reduction by H₂ at 600 °C in the pretreatment chamber of the XPS facility, which therefore avoided exposure of the samples to air prior to XPS analysis.

The NO_x-temperature-programmed desorption (NO_x-TPD) experiments,^{35, 43, 48} were carried out on the W(W/nm²CeO₂)-CeO₂ materials in a U-shape quartz reactor (13 mm i.d.). The samples were held on plugs of quartz wool, and the temperature was controlled by a Eurotherm 2408 temperature controller using a K type thermocouple. Reactant gases, used as received, were fed from independent gas cylinders (Air Liquide) by means of mass flow controllers (Brooks 5850TR) with a total flow rate of 230 mL_{NTP}/min. Prior to the NO_x-TPD experiments, the samples (0.3 g) were calcined in situ in O₂(20%)/He at 500 °C (3 °C/min) for 2 h with a flow rate of 100 mL_{NTP}/min. Typically, the composition of the adsorption mixture consisted of 400 ppm NO_x and 8% O₂ in He. The reactor outlet was continuously monitored by a chemiluminescence NO_x analyzer (Thermo Environmental Instruments 42C-HT) that allowed

the simultaneous detection of both NO and NO₂. The samples were exposed to the adsorption mixture at RT until the outlet NO_x readout was equivalent to the inlet NO_x. This latter parameter was set to ensure that saturation coverage was reached for all of the samples investigated under the present experimental conditions, as the time after which no change was observed in the gas phase NO_x concentrations was strongly dependent on the W surface density of the samples. It has been clearly demonstrated that the nature of the adsorbed NO_x species (ad-NO_x) formed on such materials is affected to a significant extent by the presence of O₂ in the NO-containing mixture.⁴⁹ As the presence of parts per million levels of O₂ cannot be excluded, NO_x adsorption and desorption were thus carried out in the presence of a large excess of O₂ (8%). Before the NO_x-TPD experiments, the samples were flushed in O₂(8%)/He (230 mL_{NTP}/min) at RT to remove weakly chemisorbed species until the NO and NO₂ concentrations detected at the outlet were negligible. NO_x-TPD experiments were carried out from RT to 550 °C at a heating rate of 3 °C/min under a mixture of 8% O₂ in He. As has already been reported in refs.^{35,43,48}, it should be noted that NO_x chemisorption does not occur on WO_x species.

N₂-FTIR spectra of adsorbed N₂ on supported Rh samples were collected in transmission mode on a Bruker Vertex 70 FTIR spectrometer equipped with a liquid N₂-cooled MCT detector and a data acquisition station. A total of 128 scans were averaged with a spectral resolution of 2 cm⁻¹. The samples were pressed into self-supporting wafers of about 12 mg/cm² (~25 mg for wafers of 1.6 cm diameter). The wafers were loaded in a moveable glass sample holder, equipped on top with an iron magnet, and inserted in a conventional quartz glass cell (CaF₂ windows) connected to a vacuum system. The iron magnet allowed for the transfer of the catalyst sample from the oven-heated region to the infrared light beam. Before N₂ adsorption, the catalysts were submitted to a dynamic (50 cm³/min) reducing pretreatment (5% H₂ in Ar, Air Liquide, 99.999%) at 600 °C for 2 h at atmospheric pressure. The samples were then evacuated (7.5×10^{-7} Torr) at 600 °C for 1 h. Finally, the temperature was decreased to -173

°C under dynamic vacuum. The samples were then exposed to 10 Torr of N₂ (Air Liquide, 99.999%) further purified by passing through a liquid nitrogen trap. The spectrum at -173 °C of the pretreated sample was used as a reference and subtracted from the spectrum of the sample exposed to N₂.

Rhodium accessibility was evaluated via the irreversible H₂ chemisorption method. These measurements were performed in a static mode using a conventional volumetric apparatus (Belsorp max, Bel Japan) and at -196 °C, as the spillover of hydrogen to the CeO₂ support has been shown to be minimized as the temperature of adsorption was lowered.²³ Typically, about 0.3 g of catalyst was used. Before the H₂ chemisorption measurements, the catalyst was reduced in H₂ (50 mL/min) at 600 °C for 2 h (3 °C/min heating rate) with subsequent evacuation at 600 °C for an additional 2 h. Then, the sample was cooled under vacuum to -196 °C. Two H₂ adsorption isotherms were obtained. After the first isotherm, the catalyst was evacuated again for 2 h at -196 °C. The amounts of total and reversible H₂ uptakes were then estimated by extrapolating the quasi-linear portions of the isotherm to zero pressure. The difference between these two values gave the amount of irreversible H₂ uptake.

Before benzene hydrogenation, the catalyst sample (0.050 g deposited on a plug of quartz wool inserted inside a U-type quartz reactor) was heated in flowing H₂ (100 mL_{NTP}/min) at atmospheric pressure with a heating rate of 3 °C/min up to 600 °C and held at this temperature for 2 h. After cooling to 50 °C under H₂, the reaction was started. The partial pressure of benzene (C₆D₆, Aldrich) was 51.8 Torr (1 Torr = 133 Pa) and the total flow rate was 107 mL_{NTP}/min with H₂ as balance. The composition of the effluent was analyzed using an online gas chromatograph (Hewlett-Packard 5890, FID) equipped with a PONA (Paraffins–Olefins–Naphthenes–Aromatics; HP, 50 m long, 0.20 mm i.d., 0.5 µm film thickness) capillary column.

A FEI Titan ETEM G2 operating at 300 kV corrected from the spherical aberration of the objective lens (Cscorrector) was used to image Rh_{Cl}/W(0.0)-CeO₂ and Rh/W(1.3)-SEA₅ under H₂ (5 to 18 mbar) and ultra-high vacuum (UHV) and/or at temperatures in the 500-1000 °C range. The environmental mode is operated by direct gas injection onto the sample. The secondary vacuum in the other parts of the microscope column is ensured by differential pumping, while the pressure around the sample can be increased up to 20 mbar. A GATAN furnace-type heating holder in Tantalum was used for the environmental experiments. In this device, the TEM grid (Mo mesh supporting a thin carbon film) is installed into a small oven surrounded by a coil. A heating rate of 50 °C min⁻¹ was used when changing the temperature during the experiments with intermediate dwelling steps for about 10 min every 100 °C up to 600 °C.

3. RESULTS

3.1. Characterization of the oxide phases

Table 1 shows that the W loadings varied from 0.0 to 15.4 wt% in the oxide samples (W(W/nm²_{CeO₂)₂)-CeO₂). After calcination at 750 °C, the BET surface area decreased slightly from 76 to 53 m²/g as the loading of W increased. This decrease in BET surface area was found to be essentially attributed to the addition of W as a rather heavy transition metal that did not provide additional surface but contributed to the increase in sample weight. The resulting W surface densities (δ) thus varied from 0.0 to 7.8 W/nm²_{CeO₂}.}

Table 1. Summary of the properties of the investigated materials

Samples	W (wt%)	Rh (wt%)	BET surface area (m ² /g)	δ (W/nm ² CeO ₂)	H/Rh	Rh dispersion estimated by EXAFS (%)
W(0.0)-CeO ₂	0.0	-	76	0.0	-	-
W(1.3)-CeO ₂	3.0	-	74	1.3	-	-
W(2.9)-CeO ₂	6.2	-	65	2.9	-	-
W(4.1)-CeO ₂	8.9	-	63	4.1	-	-
W(4.9)-CeO ₂	10.2	-	60	4.9	-	-
W(5.5)-CeO ₂	11.4	-	59	5.5	-	-
W(6.5)-CeO ₂	13.4	-	56	6.5	-	-
W(7.8)-CeO ₂	15.4	-	53	7.8	-	-
Rh/W(1.3)-SEA ₁	3.0	0.23	n.d.	1.3	0.19	100
Rh/W(1.3)-SEA ₂	3.0	0.40	n.d.	1.3	0.27	100
Rh/W(1.3)-SEA ₃	3.0	0.56	n.d.	1.3	0.32	100
Rh/W(1.3)-SEA ₄	3.0	0.71	n.d.	1.3	0.33	100
Rh/W(1.3)-SEA ₅	3.0	0.88	n.d.	1.3	0.34	100
Rh _{Cl} /W(0.0)-CeO ₂	0.0	0.94	n.d.	0.0	0.46	n.d.
Rh _{NO₃} /W(0.0)-CeO ₂	0.0	0.68	n.d.	0.0	0.47	44

3.1.1. Raman spectroscopy

Figure S1 displays the Raman spectra of the calcined oxide supports. The most intense contribution (461 cm⁻¹) is assigned to the F_{2g} symmetric breathing vibrational mode of the oxygen anions around the Ce cations (Ce-O).⁵⁰⁻⁵² The fact that this contribution did not shift with increasing W loadings (not shown) indicates that the size of the CeO₂ crystallites remained

essentially constant among the series of investigated samples.⁵³ This is supported by the quasi constant specific surface area per g of CeO₂ ($71 \pm 6 \text{ m}^2/\text{g}_{\text{CeO}_2}$) that can be calculated from the BET surface areas and the weight contents of W listed in **Table 1**. Additional contributions appeared on the introduction of W on CeO₂. At the lowest loading of W (W(1.3)-CeO₂), very weak contributions can be seen at 930 and 793 cm⁻¹ (**Figure S1**) that can be attributed to the presence of oxotungstate species (isolated monotungstates).⁴⁶ For higher W surface densities, these contributions shift to higher frequencies (979 and 803 cm⁻¹), which indicates the presence of polytungstate species in a very well dispersed state⁴⁶ and the respective contributions of W=O and W-O vibrations.⁵⁴ The fact that the W=O band becomes broader as the W surface density increases indicates a higher degree of polymerization of the polytungstates.⁵⁴ For W surface densities higher than or equal to 4.9 W/nm²_{CeO₂}, an additional contribution is observed at 690 cm⁻¹, which can be attributed to the presence of nano-crystalline WO₃ particles.^{46, 54}

3.1.2. XAS

After reduction at 600 °C, the W energy at the W-L₃ edge of the XANES of the Rh/W(1.3)-CeO₂-SEA_i samples (10.2098 keV) was found to be similar edge energy to those of the WO₃ (10.2093 keV) and Na₂WO₄ (10.2100 keV) references indicating that W is in the +6 oxidation state. The intensity of the white line and the shape of the catalysts XANES was broader and smoother than that of Na₂WO₄ consistent with a distorted coordination geometry in the former (**Figure S2a**). The W-L₃ edge EXAFS fits of the catalysts indicate there are 4.0 W-O bonds with a bond distance (1.78 Å) similar to that of Na₂WO₄ (1.78 Å). In the catalysts, the coordination geometry is more disordered than in Na₂WO₄ as indicated by a larger $\Delta\sigma^2$ fit parameter, ca. 0.004 greater than for Na₂WO₄. The first shell W-O coordination fit of magnitude and imaginary part of the k²-weighted Fourier transform of the W EXAFS is shown in (**Figure S2b**). The XANES and the EXAFS data indicate that W should be present as isolated

tetrahedrally distorted oxotungstate species in line with the Raman investigations (section 3.1.1.) and the XPS data (section 3.1.3.). Such a conclusion about the state of W on the W(1.3)-CeO₂ support is consistent with the earlier findings of Bigey et al.⁵⁵ on a WO₃-CeO₂ material exhibiting a W surface density about twice as high as that of the present studied W(1.3)-CeO₂ support.

3.1.3. XPS

The binding energy of W 4f_{7/2} in Rh/W(1.3)-SEA_i selected samples was found to be about 35 eV after calcination (**Table 2**), which can be attributed to the presence of W⁶⁺ species in agreement with the values reported on W/Ce_{0.62}Zr_{0.38}O₂ materials and those listed in earlier literature reports.^{35 and references therein} After reduction at 600 °C by H₂, the W 4f_{7/2} binding energy was found to decrease by about 0.5 eV, thus showing that the oxidation state of W did not change to a significant extent and indicating that the reduction of tungstates was not achieved under the present experimental conditions in agreement with the XAS data (section 3.1.2.). This slight change in the W 4f_{7/2} binding energy may be attributed to an electron transfer from the reduced ceria support to the tungstate species. Under ultra-high vacuum conditions, which is typically the case of the XPS chamber, the Ce⁴⁺ ions of the ceria support were found to be reduced to Ce³⁺ ions (not shown) due to the desorption of O₂. This phenomenon may also be at the origin of the slightly lower binding energy of the W 4f_{7/2} signal from the W⁶⁺ ions of tungstates supported on CeO₂ (about 35 eV) compared with those expected from pure WO₃ (35.5 eV).⁵⁶

Table 2. XPS data of selected WO_x-promoted Rh/CeO₂ Catalysts

Samples	Rh (wt%)	W 4f _{7/2} B.E. (eV)			Rh 3d _{5/2} B.E. (eV)			Rh / (W + Ce) x 10 ⁵			
		(a)	(b)	(c)	(a)	(b)	(c)	(a)	(b)	(c)	(d)
Rh/W(1.3)-SEA ₂	0.40	34.9	34.5	-	309.3	306.1	-	104	92	-	101
Rh/W(1.3)-SEA ₃	0.56	34.9	34.5	-	309.3	306.1	-	125	133	-	124
Rh/W(1.3)-SEA ₅	0.88	34.8	-	-	308.9	-	-	238	-	-	205
Rh _{Cl} /W(0.0)-CeO ₂	0.94	-	-	-	309.1	305.8	306.1 + 308.1	385	250	271	-

(a) After ex situ calcination under air at 400 °C for 2 h and exposure to ambient atmosphere.

(b) After in situ XPS reduction under H₂ at 600 °C for 2 h following step (a).

(c) After exposure to ambient atmosphere following the in situ XPS reduction in step (b).

(d) After ex situ reduction under H₂ at 600 °C for 2 h and exposure to ambient atmosphere.

3.1.4. NO_x-TPD

As illustrated earlier on Ce_{0.62}Zr_{0.38}O₂,³⁵ the NO_x-TPD profile of CeO₂ also displayed a low-temperature (LT) and a high-temperature (HT) NO_x desorption peaks at about 90 and 350 °C (not shown). The intensity of these peaks decreased as the W surface density increased and the HT desorption peak was found to vanish for W surface densities higher than or equal to 4.9 W/nm²CeO₂. As was found on ZrO₂^{43, 48} and Ce_{0.62}Zr_{0.38}O₂,³⁵ the NO_x uptake is found to decrease linearly as the W surface density increases up to about 4.9 W/nm²CeO₂ before stabilizing at higher W surface densities (**Figure S3**). From this observation it can be concluded that pseudo monolayer coverage of CeO₂ by the tungstates is achieved at a W surface density of 4.9 W/nm²CeO₂ in agreement with the values found earlier by us on Ce_{0.62}Zr_{0.38}O₂³⁵ and by Chen and co-workers on CeO₂⁵⁷ and Ce_{0.50}Zr_{0.50}O₂,⁴⁵ and in agreement with the Raman data showing the onset detection of WO₃ crystallites at such a W surface density (section 3.1.1.). Finally, the NO_x surface density found on CeO₂ (5.7 μmol NO_x/m² corresponding to 3.5 NO_x/nm²) appears to be close to those reported earlier for Ce_{0.62}Zr_{0.38}O₂ (5.3±0.3 μmol

NO_x/m^2)³⁵ and ZrO_2 ($6.0 \mu\text{mol NO}_x/\text{m}^2$).^{43, 48} It can be noted that the present results are consistent with those reported recently by Iwasaki et al.⁵⁸ These latter authors also reported a decrease in the amount of NO_x stored on ceria as the amount of W deposited increased. The slightly greater NO_x surface density reported by Iwasaki et al. for CeO_2 ($4.8 \text{ NO}_x/\text{nm}^2$)⁵⁸ compared to that obtained in the present study ($3.5 \text{ NO}_x/\text{nm}^2$) may be attributed to differences in the conditions under which CeO_2 was contacted with the NO_x species.

3.1.5. Anionic and cationic adsorption capacities

The anionic and cationic adsorption capacities of the $\text{W}(\text{W}/\text{nm}^2_{\text{CeO}_2})/\text{CeO}_2$ materials were probed by contacting 1 g of these solids with 100 mL of an aqueous solution of KCl (10^{-2} mol/L) at a pH of 4 for 1 h. The suspensions were then centrifuged and the solids were dried at 100 °C overnight before being analyzed by X-ray fluorescence. Despite Bertus and Carcel reported on a PZC of WO_3 close to 4,⁵⁹ many studies agreed that the PZC of tungsten trioxide must be below 2.^{26, 27, 60-62} Apart from few studies in which the PZC of CeO_2 has been reported to be as low as 3-4,²⁷ the PZC of ceria is generally reported to be above 6.^{26, 27, 63-65} At a pH of 4, which appears to be intermediate between the PZC of WO_3 (< 2) and that of CeO_2 (> 6),^{26, 27} the tungstates must be negatively-charged, whereas ceria must be positively-charged (**Figure 1a**). The K^+ and Cl^- ions should therefore interact preferentially with tungstates and ceria, respectively. This is verified in **Figure 1b** for which pure ceria displays only Cl^- ions after exposure to the KCl solution, whereas K^+ ions are observed on the W-promoted ceria samples only. It is of interest to note that the amount of Cl^- ions decreased drastically on the introduction of small quantities of W, becoming hardly detectable for W surface densities higher than $1.3 \text{ W}/\text{nm}^2$, and that the amount of K^+ ions increased in parallel before stabilizing for W surface densities higher than $4\text{-}5 \text{ W}/\text{nm}^2$ (**Erreur ! Source du renvoi introuvable.**). This led us to select $\text{W}(1.3)\text{-CeO}_2$ as a supporting material to achieve the selective deposition of Rh on

accessible CeO₂ via SEA of [RhCl₆]³⁻ anions (**Figure 1a**). In agreement with the lack of anionic adsorption capacity of W(2.9)-CeO₂ (**Figure 1b**), it was verified that Rh could not be deposited on this latter support under the SEA conditions used in the present work (pH 4).

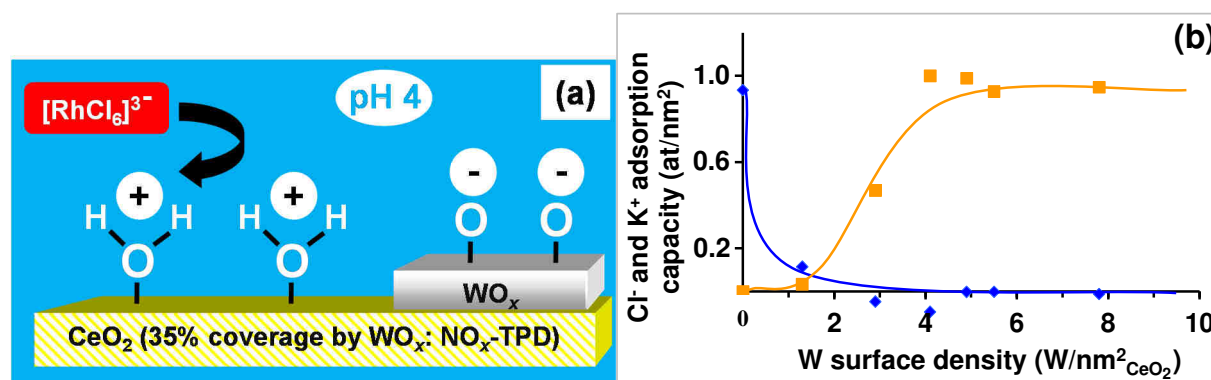


Figure 1. (a) Schematic representation of the selective interaction of the anionic Rh precursor ([RhCl₆]³⁻) with the W(1.3)-CeO₂ support in the course of the 1st SEA step via electrostatic attraction between ceria surfaces and the charged precursor in solution at a pH of 4. The charge state shown in the figure represents a net charge of WO_x and CeO₂ surface after protonation/deprotonation at a pH of 4. (b) Anionic (Cl⁻, orange) and cationic (K⁺, blue) adsorption capacities of W(W/nm²_{CeO₂})-CeO₂.

3.2. Characterization of the Rh phases

The deposition of Rh on the W(1.3)-CeO₂ support was performed by successive SEA experiments of [RhCl₆]³⁻ anions at a pH of 4, for which accessible CeO₂ must be charged positively, whereas tungstates must be charged negatively. Such a procedure should therefore allow for the selective electrostatic interaction of the [RhCl₆]³⁻ complex with the positively-charged CeO₂ surface (**Figure 1a**). From the data listed in **Table 1**, it can be seen that the amount of Rh deposited on the W(1.3)-CeO₂ support increases up to 0.88 wt% as the number

of successive SEA experiments increases. The amounts of Rh deposited for Rh_{Cl}/W(0.0)-CeO₂ and Rh_{NO₃}/W(0.0)-CeO₂ were estimated to be 0.94 and 0.68 wt%, respectively.

3.2.1. Hydrogen chemisorption

The H/Rh ratios obtained for the various Rh samples after reduction and evacuation at 600 °C are listed in **Table 1**. It was found that this ratio remained low and increased from 0.19 to 0.34 as the number of successive SEA processes increased. Yet the H/Rh ratio was found to remain essentially constant (0.33 ± 0.01) after the third SEA step. H/Rh ratios of the Rh samples prepared on the W-free support (W(0.0)-CeO₂) were found to be independent of the Rh precursor, as Rh_{Cl}/W(0.0)-CeO₂ and Rh_{NO₃}/W(0.0)-CeO₂ exhibited H/Rh ratios of 0.46 and 0.47 (**Table 1**), respectively. These latter H/Rh ratios were thus found to be higher than those of the Rh samples prepared on W(1.3)-CeO₂.

3.2.2. XAS

As illustrated for Rh/W(1.3)-SEA₅ in **Figure 2a**, the XANES spectra recorded on the Rh/W(1.3)-SEA_i samples at the Rh-K edge after H₂ reduction at 600 °C (**Figure S4a**) indicate that Rh was present in a metallic state. The XANES energy of the catalysts and Rh foil is 23.220 keV. The magnitude of the k²-weighted Fourier transform of the EXAFS is shown in (**Figure 2b**) and indicates that the Rh nano-particles are small. As listed in **Table 3**, the Rh-Rh coordination numbers (CN) in the Rh/W(1.3)-SEA_i series, deduced from fitting the k²-weighted EXAFS spectra were found to be extremely low (ca. 4) and to remain essentially constant through the series. In contrast, the sample prepared from a W-free CeO₂ support (Rh_{NO₃}(0.68)/W(0.0)-CeO₂, **Table 3** and (**Figure 2b**)) showed a higher coordination number (7.3), albeit still low. In agreement with the observed low coordination numbers, a small contraction of the Rh-Rh bond distance by about 0.04 ± 0.01 Å was found for the studied

samples compared to that found for the Rh foil (2.69 Å). From these EXAFS coordination numbers, the size of the Rh particles was estimated and is also listed in **Table 3**. The associated Rh dispersion (defined as the fraction of surface Rh atoms to the total number of Rh atoms) was thus estimated to be 100 % (**Table 1**) suggesting full dispersion of the Rh atoms in the Rh/W(1.3)-SEA_i series. Whereas the Rh dispersion of Rh_{NO3}/W(0.0)-CeO₂ estimated by EXAFS (44 %) agreed remarkably with that determined by H₂ chemisorption (H/Rh = 0.47), this was definitely not the case in the Rh/W(1.3)-SEA_i series for which Rh dispersions determined by H₂ chemisorption were found to be much lower than those deduced from EXAFS (**Table 1**).

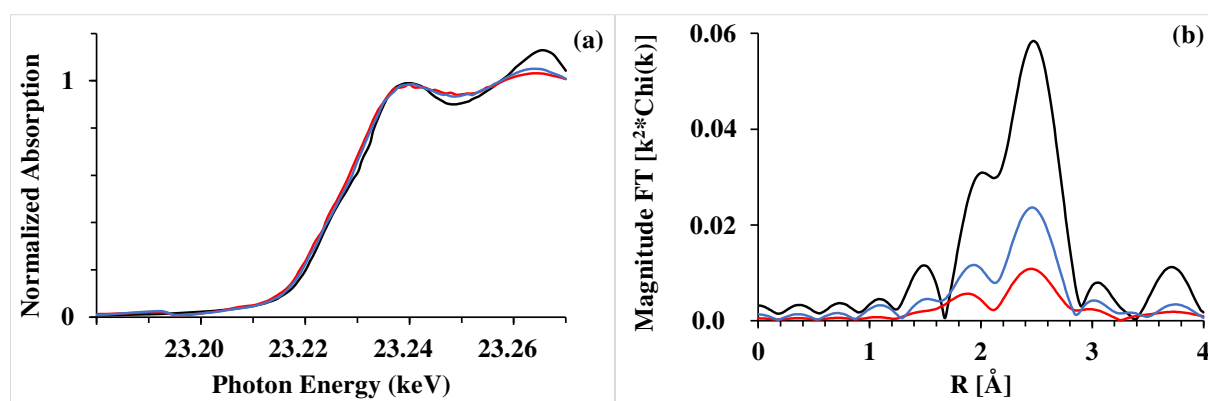


Figure 2. (a) Rh K-edge XANES spectra recorded from 23.18 to 23.27 keV of Rh foil (black), Rh/W(1.3)-SEA₅ (red) and Rh_{NO3}/W(0.0)-CeO₂ (blue). (b) The magnitude of the k^2 -weighted Fourier transform of Rh K-edge EXAFS spectra ($\Delta k = 2.8$ - 11.4 \AA^{-1} and $\Delta R = 1.3$ - 2.8 \AA) of Rh foil (black), Rh/W(1.3)-SEA₅ (red) and Rh_{NO3}/W(0.0)-CeO₂ (blue). The spectra of the supported Rh samples were recorded at room temperature after reduction in flowing H₂ at 600 °C.

Table 3. Rh k-edge EXAFS fits of WO_x-promoted Rh/CeO₂ Catalysts

Samples	CN	R (Å)	$\Delta\sigma^2$ ($\times 10^3$)	E ₀ (eV)	Size (nm)
---------	----	-------	------------------------------------	---------------------	-----------

Rh/W(1.3)-SEA ₁	3.8	2.65	5.0	0.9	0.8
Rh/W(1.3)-SEA ₂	3.7	2.64	5.0	-0.6	0.8
Rh/W(1.3)-SEA ₃	4.2	2.65	5.0	-0.2	0.9
Rh/W(1.3)-SEA ₄	3.9	2.65	5.0	0.5	0.9
Rh/W(1.3)-SEA ₅	4.0	2.66	5.0	0.9	0.9
Rh _{NO₃} /W(0.0)-CeO ₂	7.3	2.67	4.0	-0.8	2.5
Rh foil	12.0	2.69	0.0	-0.7	-

CN, the average Rh-Rh coordination number; R, the distance between Rh scattering atoms and their 1st neighboring Rh atoms; $\Delta\sigma^2$, the Debye-Waller factor measuring the disorder, E₀, the correction on the edge position.

3.2.3. XPS

The Rh/W(1.3)-SEA_i samples were firstly reduced at 600 °C under H₂ and exposed to air before introduction in the XPS facility. **Figure 3** shows the theoretical (●) and XPS (○) Rh/(W + Ce) atomic ratios determined on the Rh/W(1.3)-SEA_i series. The XPS ratios were found to be higher than the theoretical ones. This is not unexpected as in the case of well-dispersed metal particles, the proportion of Rh atoms analyzed by XPS is known to be greater than the proportion of Ce atoms analyzed from support particles whose sizes are significantly larger (ca. 11 nm from the specific surface area of CeO₂) than those of the Rh particles.²³ The XPS Rh/(W + Ce) ratios were found to be remarkably proportional to the Rh weight loadings, which suggests that Rh was present in a highly dispersed state in this series of samples in agreement with the XAS results (section 3.2.2.). The oxidation state of W and Rh was investigated for selected samples (Rh/W(1.3)-SEA₂, Rh/W(1.3)-SEA₃, Rh/W(1.3)-SEA₅ and Rh_{Cl}/W(0.0)-CeO₂) which were analyzed in their oxidized form (after ex situ calcination at 400

°C), after reduction by H₂ at 600 °C in the pretreatment chamber of the XPS facility (no exposure to air after the in situ reduction step) and after further exposure to air of some of the in situ reduced samples. The binding energy of Rh 3d_{5/2} was found to be about 309 eV after calcination (**Table 2**, (a), **Figure S5a**), attesting for the presence of Rh³⁺ species in agreement with the values reported on W/Ce_{0.62}Zr_{0.38}O₂ materials³⁵ and those listed in earlier literature reports.⁶⁶ After in situ reduction at 600 °C by H₂, the Rh 3d_{5/2} binding energy was found to decrease to about 306 eV (**Table 2**, (b), **Figure S5b**) thus showing that the Rh³⁺ ions were reduced to Rh⁰ metal atoms.³⁵ After exposure to air of the in situ reduced Rh_{Cl}/W(0.0)-CeO₂ sample, an additional contribution appeared at about 308 eV suggesting partial reoxidation of the Rh atoms (**Table 2**, (c), **Figure S5c**). The Rh/(W + Ce) ratios of the oxidized and in situ reduced Rh/W(1.3)-SEA₂ and Rh/W(1.3)-SEA₃ samples (**Table 2** (a,b)) were found to be consistent with those obtained with ex situ reduction (**Table 2** (d) and **Figure 3**). In contrast the Rh/(W + Ce) ratio of the Rh_{Cl}/W(0.0)-CeO₂ in its oxidized form appeared to be much greater than that in its in situ reduced form (**Table 2** (a,b)). This suggests that Rh sintering occurred during the reduction step on the W-free sample (Rh_{Cl}/W(0.0)-CeO₂), whereas this sintering phenomenon did not occur on the samples prepared on the tungstated support (Rh/W(1.3)-SEA_i).

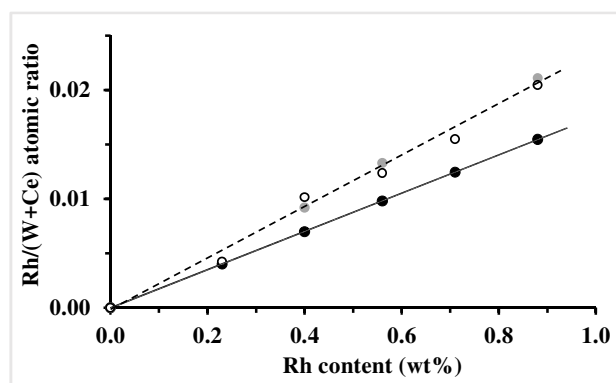


Figure 3. XPS Rh/(W + Ce) atomic ratios as a function of the Rh loading of the Rh/W(1.3)-SEA_i series, theoretical (●), after ex situ H₂ reduction (○) and after in situ H₂ reduction (●).

3.2.4. N₂-FTIR

Although less sensitive than CO and more technically demanding (elevated pressure or low temperature required),⁶⁷ N₂ was preferred to CO to characterize the Rh atoms of the Rh/W(1.3)-SEA_i series, since N₂ does not alter the integrity of the Rh particles upon adsorption and its stretching vibration is not dipole-dipole coupling-dependent as is the case with CO.⁶⁸ The negative and positive contributions observed at 2120 and 2090 cm⁻¹, respectively, have been attributed to a shift of the contribution at 2120 cm⁻¹ (assigned to f centers in reduced ceria⁶⁹) to lower wavenumbers with a further decrease in the temperature of the self-supporting wafer upon the introduction of the N₂ atmosphere (**Figure S6a**).⁷⁰ Whereas the band at 2335-2340 cm⁻¹ (not shown) is assigned to the interaction of N₂ with the hydroxyl groups of the supporting oxide, those at 2200, 2215 and 2250 cm⁻¹ (**Figure S6a**) are assigned to the vibration of N₂ chemisorbed onto Rh sites.⁷⁰ The two most intense bands at 2200 and 2215 cm⁻¹ are assigned to the vibration of N₂ molecules chemisorbed on metallic rhodium (Rh⁰) atoms, while that at 2250 cm⁻¹ of much weaker intensity is attributed to N₂ bonded to electron-deficient Rh atoms (Rh^{δ+}).^{70, 71} It can be seen that the intensity of the N₂ contributions assigned to the chemisorption of N₂ on Rh⁰ atoms increases to a larger extent than that of N₂ bonded to Rh^{δ+} sites suggesting that Rh atoms are essentially present as Rh⁰ sites as the Rh content increases. The N₂-Rh⁰ contributions of the Rh/W(1.3)-SEA_i series (2200 and 2215 cm⁻¹) appears at about 10 cm⁻¹ lower wavenumbers than those recorded previously on Rh/SiO₂ samples (2210 and 2225 cm⁻¹), for which no electronic transfer is known to occur between the Rh particles and the SiO₂ support.⁷¹ The fact that the N₂-Rh⁰ contributions of the Rh/W(1.3)-SEA_i series appears at lower wavenumbers than that of Rh/SiO₂ may be attributed to increased electron density of the Rh particles because of an electronic transfer from the reduced ceria support leading to a higher

electron back donation in the $2\Pi^*$ anti-bonding N_2 orbital. **Figure S6b** shows the comparison of $Rh_{Cl}/W(1.3)-CeO_2$ with $Rh/W(1.3)-SEA_3$ recorded within the same series of experiments. It can be seen that the resolution of the contributions at about 2000 and 2010 cm^{-1} appeared higher on $Rh_{Cl}/W(1.3)-CeO_2$ compared to $Rh/W(1.3)-SEA_3$, thus suggesting that the morphology of the Rh particles must be different on these samples.

3.2.5. Benzene hydrogenation catalytic results

The benzene hydrogenation rates, normalized per g of Rh in the samples, and associated turnover frequencies (TOF⁷² defined as the number of benzene molecules converted per time and per Rh surface atom by considering the H/Rh data derived from H_2 chemisorption experiments) measured on the various samples are shown in **Figure 4**. Regarding firstly the $Rh/W(1.3)-SEA_i$ series, it can be seen that the benzene hydrogenation rate increases as the Rh content increases before stabilizing for Rh contents greater than or equal to 0.56 wt%, in other words after three successive SEA synthesis steps. The benzene hydrogenation rates of the W-free samples, namely $Rh_{NO_3}/W(0.0)-CeO_2$ and $Rh_{Cl}/W(0.0)-CeO_2$, not only were found to be similar for both samples but also greater than those measured on the $Rh/W(1.3)-SEA_i$ series. These differences in benzene hydrogenation rates disappear when the TOF are considered as all of these catalysts exhibit a benzene hydrogenation TOF of $0.12 \pm 0.03 s^{-1}$. This value is in good agreement with that reported earlier for $Rh/WO_x-Ce_{0.68}Zr_{0.32}O_2$ samples at low tungstate coverages.³⁵

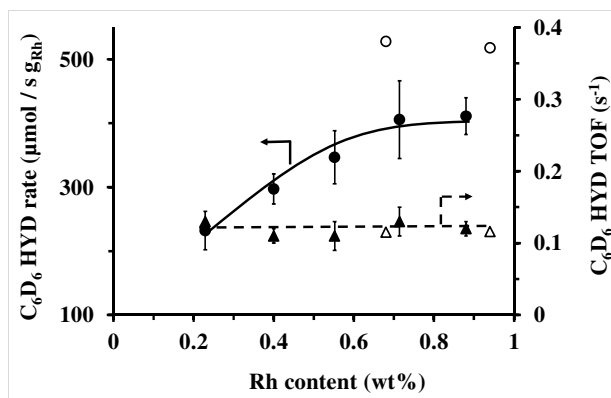


Figure 4. C_6D_6 hydrogenation rates (circles) and C_6D_6 hydrogenation TOF (triangles) as a function of the Rh content in the Rh/W(1.3)-SEA_i series (0.23-0.88 wt% Rh) (full symbols), and RhNO₃/W(0.0)-CeO₂ (0.68 wt% Rh) and RhCl/W(0.0)-CeO₂ (0.94 wt% Rh) (open symbols).

4. DISCUSSION

4.1. Formation and atomicity of the Rh₂O₃ clusters prepared by successive SEA of [RhCl₆]³⁻ on W(1.3)-CeO₂

The synthesis of the samples of interest lies in the selective deposition of Rh on the accessible surface of CeO₂ of a tungstated-ceria support. To achieve this goal, the method based on the strong electrostatic adsorption (SEA) of a negatively-charged Rh precursor with the CeO₂ surface was selected. This method is based on the points of zero charge (PZCs) of the oxides of interest, namely CeO₂ (PZC > 6) and WO₃ (PZC < 2).^{26, 27} For a single oxide, setting the pH of the aqueous medium to a value lower than that of the PZC of the oxide will result in the protonation of the OH groups of this oxide eventually creating positively-charged adsorption sites able to interact with anionic species. In contrast, when the pH of the adsorption medium is set to a value greater than that of the PZC of the oxide, the deprotonation of the OH groups of the oxide will result in the creation of negatively-charged adsorption sites able to interact with cationic species. In the case of materials made of two oxides, the same surface

charging will apply when the pH of the adsorption medium is set below and above the lower and the higher PZC of the constitutive oxides, respectively. In contrast, setting the pH of the adsorption medium to a value intermediate to those of the PZCs of the oxides will create positively- and negatively-charged adsorption sites on the oxides exhibiting the greater and lower PZC, respectively. In that case, the choice of an appropriate metal complex, either anionic or cationic, will allow its selective deposition on one of these oxides. Contacting the W(1.3)-CeO₂ material with an adsorption medium at a pH of 4 containing the negatively-charged hexachlororhodate complex ([RhCl₆]³⁻) should thus result in its selective interaction with the positively-charged adsorption sites of CeO₂ (PZC > 6). In contrast, this Rh complex should not interact with the negatively-charged sites created on the tungstates (PZC < 2) because of repulsive interaction of the negatively-charged sites and the anionic precursor of Rh (**Figure 1a**).

The coverage of CeO₂ by the tungstates in the W(1.3)-CeO₂ material was estimated to be about 35 % from the data recorded by the NO_x-TPD method (**Figure S3**). This technique provides a reliable estimation of the coverage of CeO₂ by the tungstates, as monolayer coverage was deduced to be about 4.9 W/nm² in agreement with earlier reports,^{45, 57} which supports the appropriateness of the synthesis method used to prepare the tungstated materials. The NO_x-TPD characterization technique appears to be limited, however, in predicting the tungstate coverage that should be used for the selective deposition of a metal complex in an aqueous medium as the CeO₂ adsorption sites in solution may be differently influenced by the tungstates compared to those involved in the adsorption of NO_x from a gaseous medium. A more reliable descriptor of the influence of increasing quantities of tungstates supported on CeO₂ on the adsorption properties of the underlying support shall be assessed by the determination of the cationic and anionic adsorption capacities of the tungstated materials in a liquid medium at a pH of 4 (**Figure 1b**). These data show that the anionic adsorption capacity of ceria decreases drastically on the

introduction of small quantities of W as the W(1.3)-CeO₂ sample exhibit about 12 % of the anionic adsorption capacity of pure CeO₂ and that the anionic adsorption capacity appears to be vanishing for W(2.9)-CeO₂. These data led us to select the W(1.3)-CeO₂ material as a supporting oxide for the selective adsorption of Rh on the accessible CeO₂ surface via the SEA process. As shown in **Table 1**, the amount of Rh deposited on the W(1.3)-CeO₂ support increases as the number of successive SEA increases. The amount of Rh deposited after the first SEA process was found to be 0.23 wt% Rh (**Table 1**, Rh/W(1.3)-SEA₁). It must be highlighted that full deposition of Rh (0.94 wt% Rh, 0.72 Rh at/nm²) was achieved when contacting CeO₂ with an ammonium hexachlororhodate hydrate solution (Rh(0.94)/W(0.0)-CeO₂ sample). In agreement with the anionic adsorption capacity of W(1.3)-CeO₂ (**Figure 1b**), this clearly indicates that tungstates decreased drastically the number of adsorption sites of CeO₂ able to interact electrostatically with the hexachlororhodate complex, as the Rh deposited onto the sample submitted to the first SEA process amounted to 0.23 wt% only. Such a deposition of Rh in the course of the first SEA process can be estimated to be about 0.18 Rh at/nm², which is found to compare reasonably well with the 0.12 Cl at/nm² deposited on the W(1.3)-CeO₂ support in the anionic adsorption capacity experiment (**Figure 1b**). It must also be recalled that the obvious differences in negative charge and size of the hexachlororhodate complex compared with those of chlorides are thought to be at the origin of additional complexity in the comparison of the interaction of the [RhCl₆]³⁻ and Cl⁻ anions with the positively-charged CeO₂ surface of W(1.3)-CeO₂. Four successive strong electrostatic adsorptions were then carried out starting from Rh/W(1.3)-SEA₁ with intermediate calcination steps at 400 °C and this resulted in an increase in the amount of Rh deposited on W(1.3)-CeO₂ after each SEA process up to 0.88 wt% after the fifth SEA experiment (**Table 1**). It must be highlighted here that the use of successive SEA processes in order to increase the metal loading on a support has only been reported once to the best of the authors knowledge. In this particular work, Job et al. were able to increase the

amount of Pt deposited on a carbon xerogel support by repeating the SEA deposition process up to three times with intermediate reduction of the Pt precursor between the successive SEA processes.⁷³ As far as we know, intermediate calcination between successive SEA processes, as done in the present study, has not previously been reported and potentially brings about additional complexity as Rh₂O₃ clusters must be formed during this step as indicated by a Rh 3d_{5/2} binding energy of about 309 eV⁷⁴ (**Table 2**), whereas that of RhCl₃ is expected at about 310 eV.^{19, 75, 76} The PZC of Rh₂O₃ has been reported to be about 9.⁷⁷ As the pH of the adsorption medium was set to 4 in the successive SEA steps, the formed Rh₂O₃ clusters should also be positively-charged, as is the case of CeO₂, and therefore be able to interact electrostatically with the Rh anionic complex. Of particular interest is that the amount of Rh deposited in the successive SEA experiments, namely from the second to the fifth one, was found to remain essentially constant (0.16 ± 0.1 wt%) in this series (**Table 1**). This suggests firstly that the Rh anionic complex should only be interacting with the Rh₂O₃-like clusters to a minimal extent. This essentially constant Rh deposition also indicates that about 30 % ((0.23-0.16)/0.23) of the cationic adsorption sites of CeO₂ of the W(1.3)-CeO₂ oxide were no longer accessible to the interaction with the Rh anionic complex after calcination very likely because of being in close interaction with Rh₂O₃ clusters, the presence of which is supported by a Rh 3d_{5/2} binding energy of about 309 eV (**Table 2**) in the calcined samples (section 3.1.3.). This result differs substantially from that reported by Job et al. as these authors concluded to the complete regeneration of the adsorption sites of a carbon material after a reduction step.⁷³ In contrast, the present study shows that only 70 % (0.16/0.23) of the cationic adsorption sites of CeO₂ are found to be regenerated by the calcination step as schematically represented in **Figure 5**. The Rh anionic complex should therefore interact with the fraction of cationic adsorption sites of CeO₂ regenerated by the calcination steps preceding subsequent SEA steps. It can also be deduced from these data that the Rh₂O₃ clusters formed after calcination for the material issued

from the first SEA experiment (Rh(0.23)/W(1.3)-SEA₁) should exhibit an average atomicity, referred to as the average number of Rh atoms per Rh₂O₃ cluster, of about 3.5 Rh atoms (surface density of Rh atoms / surface density of “lost” adsorption sites = 0.23/0.065). Similarly, an atomicity of 6.1, 8.4, 10.8 and 13.3 Rh atoms in Rh₂O₃ clusters can be estimated on Rh(0.40)/W(1.3)-SEA₂, Rh(0.56)/W(1.3)-SEA₃, Rh(0.71)/W(1.3)-SEA₄ and Rh(0.88)/W(1.3)-SEA₅, respectively, after calcination. These data also suggest that the number of Rh₂O₃ clusters should remain essentially constant over the Rh/W(1.3)-SEA_i series of samples, whereas the Rh atomicity of the Rh₂O₃ nanoparticles increases as the amount of Rh in these samples increases. The present method consisting in performing successive SEA experiments of the Rh anionic complex with the positively-charged CeO₂ surface of a W(1.3)-CeO₂ support, with intermediate calcination between each SEA experiment, can therefore be described as a nucleation-growth process of the Rh₂O₃ clusters (**Figure 5**). The surface density of the nucleation sites of the Rh₂O₃ clusters can be straightforwardly quantified from the amount of the [RhCl₆]³⁻ adsorption sites that were not regenerated by calcination after the first SEA step per unit surface area of CeO₂ in the W(1.3)-CeO₂ pristine support. This density, estimated to be about 0.05 nucleation site /nm²_{CeO₂} (0.065 / 100 / 102.91 x 6.02 x 10²³ / (76 x 10¹⁸)), appears to be about 3.5 times lower than that of the Rh surface density (0.18 Rh/nm²_{CeO₂}) after the first SEA step in agreement with the deduced atomicity of the Rh₂O₃ clusters on Rh/W(1.3)-SEA₁.

Computational studies concluded to a relatively strong interaction of the RhO_x clusters with the CeO₂ (111) surface,⁷⁸⁻⁸⁰ in line with HRTEM observations,⁷⁹ leading to the formation of two-dimensional (2D) clusters/films. The formation of such 2D clusters would be at the origin of their pronounced resistance to sintering under oxidizing conditions⁷⁹ in agreement with the earlier statements of Van Delft and Nieuwenhuys for oxide layers on reducible supports.⁸¹

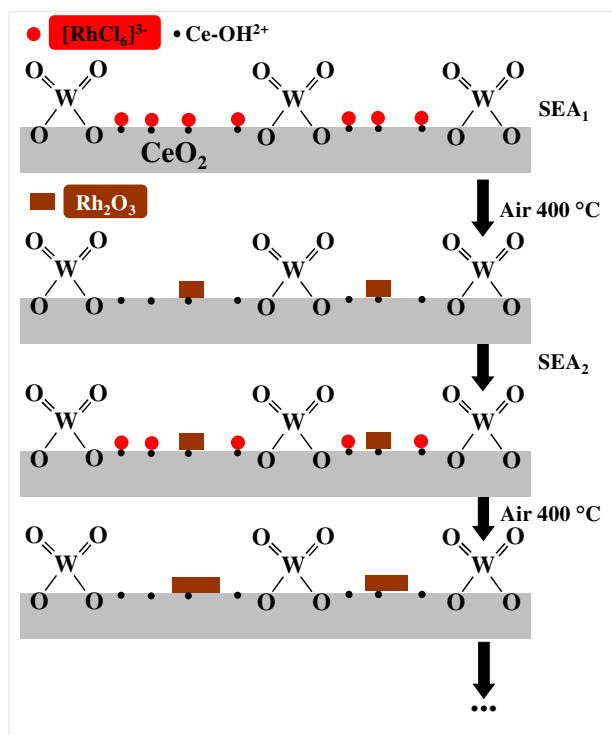


Figure 5. Schematic representation of the successive SEA steps and the associated nucleation-growth of Rh_2O_3 films over the $W(1.3)-CeO_2$ supporting oxide to produce the $Rh/W(1.3)-SAE_i$ materials in their calcined state.

4.2. Can strong metal-support interaction (SMSI) be at the origin of the evolution of the Rh weight-normalized benzene hydrogenation rates over the $Rh/W(1.3)-SAE_i$ series?

It must be emphasized that the benzene hydrogenation rates (normalized per g of Rh) were found to increase as the number of successive SEA increases (**Figure 4**), in other words as the Rh content in the SEA samples increases. This clearly indicates that the increase in the benzene hydrogenation rate cannot be attributed to an increase in the density of Rh clusters of equivalent average size, as the latter hypothesis should have resulted in an essentially constant benzene reaction rate normalized per g of Rh over this series of samples. One may argue that this increase in normalized benzene hydrogenation rate over the $Rh/W(1.3)-SEA_i$ series could

be attributed to a lowering of strong metal-support interaction (SMSI) effect of CeO₂ with an increase in the Rh particle size as the Rh content increases, even if such an increase in the Rh particle size appears unlikely from the XAS (section 3.2.2.) and XPS (section 3.2.3.) data. Tauster originally highlighted that SMSI resulted in the suppression of the hydrogen adsorption capacity of group VIII metals supported on TiO₂ after high reduction temperature.⁸² SMSI was essentially attributed to a geometric effect with the coverage of the metal particles by TiO_x species from the support.⁸³ SMSI has been claimed to occur with Ni,⁸⁴ Pd,⁸⁵ and Rh⁸⁶ supported on CeO₂ after reduction by H₂ at relatively moderated temperatures. Barrault et al. reported on an almost complete loss of H₂ chemisorption and benzene hydrogenation activity on Ni(7.5%)/CeO₂ after reduction at 400 °C, whereas this was not found to be the case after reduction at 250 °C.⁸⁴ The existence of such a SMSI effect was latter discarded after reduction at moderate temperatures for CeO₂-supported Rh catalysts.^{37, 87-90} No decoration of the Rh particles by CeO_x moieties could be observed up to reduction temperatures as high as 500 °C and the metal support interaction was rather attributed to an epitaxial relationship between the Rh particles and the CeO₂ support.^{37, 87, 88} After reduction at 500 °C, the much stronger reduction in the chemisorption capacity of the sample prepared with a high surface ceria support (Rh/CeO₂ (HS)), compared to that of the sample prepared with a low surface support (Rh/CeO₂ (LS)), was attributed to the sintering of CeO₂ (HS) and the burial of Rh into the sintered support.⁸⁷ The metal particle decoration phenomenon was demonstrated to occur after reduction at 700 °C for Rh/CeO₂³⁶ and 900 °C for Pt/CeO₂,⁹¹ whereas such a SMSI effect was shown to be absent up to reduction temperatures as high as 550 °C in the latter study. In addition to this, the benzene TOF (C₆D₆ HYD TOF, **Figure 4**, triangles) calculated on the basis of the normalized benzene hydrogenation rates (**Figure 4**) and the H/Rh data (**Table 1**) were found to remain essentially constant ($0.12 \pm 0.03 \text{ s}^{-1}$) over Rh_{Cl}/W(0.0)-CeO₂, Rh_{NO₃}/W(0.0)-CeO₂ and the Rh/W(1.3)-SEA_i series. The latter TOF is found to be in excellent agreement with the TOF

value that could be extrapolated to 0.15 s^{-1} at a temperature of $50 \text{ }^\circ\text{C}$ from the data of Bernal et al. ($0.16 \text{ mmol (C}_6\text{H}_{12}) \text{ g}^{-1} \text{ (Rh) s}^{-1}$ at $30 \text{ }^\circ\text{C}$, $\text{H/Rh} = 0.27$) over a $\text{Rh}(2.4 \text{ wt}\%)/\text{CeO}_2$ (LS) reduced at $500 \text{ }^\circ\text{C}$,³⁷ for which no SMSI is anticipated,^{37, 87, 88} and by considering an activation energy of the benzene hydrogenation reaction of 37 kJ/mol .⁹² The drastic decrease in the TOF (0.03 s^{-1}) extrapolated from the data of Bernal et al. over a $\text{Rh}(2.9 \text{ wt}\%)/\text{CeO}_2$ (HS) may be more likely attributed to the burial of Rh in the sintered support (decrease in the specific surface area by a factor of 2 after reduction at $500 \text{ }^\circ\text{C}$).⁸⁸ Moreover, the TOF recorded in the present study is found to agree with those reported earlier for Rh supported non-reducible oxides (0.22 s^{-1}).^{92, 93} Considering (i) the calcination step to $700 \text{ }^\circ\text{C}$ of the pristine CeO_2 support prior W and Rh deposition (section 2.1.), which should thus prevent further sintering of the support during the reduction step at $600 \text{ }^\circ\text{C}$, (ii) the lower reduction temperature used in the present work compared to that for which the SMSI phenomenon has been shown to occur for Rh supported on CeO_2 -related samples in earlier studies ($700 \text{ }^\circ\text{C}$),^{36, 94} (iii) the fact the SMSI effect was claimed to be less pronounced with a chloride Rh precursor,⁹⁵ which is the case in the present study where $(\text{NH}_4)_3\text{Rh}(\text{Cl}_6)$ was used in the SEA processes, (iv) the essentially constant TOF for all of the samples evaluated in the present work, in good agreement with earlier data for which no SMSI could be anticipated^{87, 92, 93} and (v) the close agreement between the H/Rh ratio (0.47) and the Rh dispersion estimated by EXAFS (44 %) for $\text{RhNO}_3/\text{W}(0.0)\text{-CeO}_2$ (**Table 1**), which further supports the reliability of the chemisorption method used in the present work, the occurrence of a SMSI effect to account for the observed increase in the normalized benzene hydrogenation rates as the Rh content increases over the $\text{Rh}/\text{W}(1.3)\text{-SEA}_i$ series (**Figure 4**) can be ruled out.

The increase in benzene hydrogenation rate normalized per g of Rh (**Figure 4**), together with the increase in the H/M ratio (**Table 1**), as the Rh content increases may be more likely attributed to Rh metallic clusters of very low atomicity, as indicated by the extremely low

coordination numbers determined by EXAFS (**Table 3**, $CN = 4.0 \pm 0.2$) found for the Rh clusters produced by the particular successive SEA processes.

4.3. Atomicity of the Rh clusters after high temperature reduction

As the Rh/(W+Ce) XPS ratios of the calcined samples were found to be fairly consistent with those of the reduced samples and to be proportional to the amount of Rh deposited in the course of the SEA processes (**Table 2** and **Figure 3**), it can be argued that the size of the Rh metal clusters should not have resulted from pronounced sintering after reduction under H_2 at 600 °C and should have remained in a highly dispersed state over the W(1.3)-CeO₂ support. In contrast, the Rh/(W+Ce) XPS ratio of the calcined Rh_{Cl}/W(0.0)-CeO₂ sample was found to decrease to a significant extent after reduction at 600 °C (**Table 2**), thus suggesting that Rh sintered to a much greater extent during the reduction step on the W-free CeO₂ support. The conclusion that the presence of tungstates drastically limited the sintering of Rh during the reduction step is further supported by the much lower coordination numbers ($CN = 4.0 \pm 0.2$) and associated Rh particle size deduced from the XAS experiments over the Rh/W(1.3)-SAE_i series compared to the W-free RhNO₃/W(0.0)-CeO₂ sample ($CN = 7.3$, **Table 3**).

The absence of second Rh shell in the EXAFS spectra (**Figure 2b**) in the Rh/W(1.3)-SAE_i series also supports the presence of Rh clusters of very low atomicity in agreement with the very low average CN found for this series of samples (**Table 3**). In contrast, the absence of any oxygen contribution at low distance is more puzzling as the formed Rh clusters should be lying onto the CeO₂ surface. It must be recalled that the XAS measurements were carried out at RT after reduction at 600 °C under flowing H_2 (section 2.2.). Under such in situ experimental conditions, CeO₂ must be deeply reduced and its surface highly deficient in terms of O species.^{22, 23}

Considering all of the above, the atomicity of the Rh_2O_3 clusters deduced from the chemical analyses of the samples prepared by the successive SAE processes (section 4.1.) in their calcined state was considered as a basis for the proposal of the Rh metal model clusters (section 4.4.). In these models, the atomicity of the Rh metal clusters was set by rounding those deduced for the RhO_x clusters, namely 3.5, 6.1, 8.4, 10.8 and 13.3 for the Rh/W(1.3)-SEA_i series (section 4.1.), to the closer integer, i.e. 4, 6, 8, 11 and 13 Rh atoms per metal cluster, which will be referred to as to Rh₄, Rh₆, Rh₈, Rh₁₁ and Rh₁₃, respectively.

The existence of clusters of very low atomicity has been claimed in earlier studies performed on Pt/ Al_2O_3 ,^{17, 19} Pt/ FeO_x ,¹⁰ Rh/ SiO_2 ,⁹⁶ Rh/ Al_2O_3 ^{16, 18, 97} and Rh/ CeO_2 .^{78, 98} Most of these studies share the common feature of using metal loadings well below 1 wt% as is the case in the present study. When the Rh loading was greater, Jeong et al. had to perform a high-temperature hydrothermal treatment to achieve high Rh dispersion on CeO_2 .⁹⁸ In these studies, the atomicity of the corresponding metal clusters was claimed to be 11,¹⁹ 12-20,¹⁷ < 10,¹⁰ for Pt samples, and 8,¹⁶ 6-10⁹⁷ and < 10⁹⁸ for Rh samples on the basis of HRTEM^{10, 16, 17} and/or EXAFS measurements for which very low average coordination numbers were reported such as 3.8,¹⁰ 3.8¹⁹ and 3.7,⁹⁷ in agreement with those found in the present study (**Table 3**).

4.4. Proposal of model Rh clusters

Figure 6 describes the Rh clusters that were considered according to the atomicity listed in section 4.3. Model 3D_1 is based on a hexagonal assembly of the Rh atom on a three-dimensional (3D) symmetry on a (111) CeO_2 surface with the highest possible Rh stacking, to mimic what can be found in common metal particles. Models 3D_2 and 3D_3 are also based of

three-dimensional clusters but limited to two layers of Rh atoms either assembled along (111) or (100) surfaces and limited to two rows of Rh atoms (**Figure 6a**), respectively. Model 3D_2 would be consistent with the Rh₇ cluster lying on a (111) Al₂O₃ surface proposed by van 't Blik et al. to account for the very low average coordination number of 3.7 found on a Rh(0.57 wt%)/Al₂O₃ sample by these authors.⁹⁷ The last 3D model (3D_4), is based on the theoretical study of Song et al.⁷⁸ These authors calculated the most stable structures of Rh clusters with atomicities ranging from 1 to 10 Rh atoms on a clean CeO₂(111) surface. In this model, Rh₁₁ (**Figure 6a, i**) and Rh₁₃ (**Figure 6a, ii and iii**) clusters were proposed on the basis of the Rh₁₀ cluster reported by Song et al.⁷⁸ to which 1 and 3 Rh atoms were added, respectively.

As the presence of Rh rafts was also claimed in earlier studies,^{10, 16-19} 2D model clusters were also considered (**Figure 6b**). These models can be described as one layer-thick clusters based on (111) (Models 2D_1 and 2D_2) and (100) (Model 2D_3) symmetries. Model 2D_2 was considered based on the computational study of Piotrowski et al. in which it was claimed that Rh₄ was present as 2D arrays with a zigzag orientation on (111) CeO₂ surface,⁹⁹ whereas Model 2D_3 is related to the work of Vaarkamp et al. who reported on Pt₁₁(100) rafts on Al₂O₃ to account for the average coordination number of 3.8 after H₂ reduction at 450 °C.¹⁹

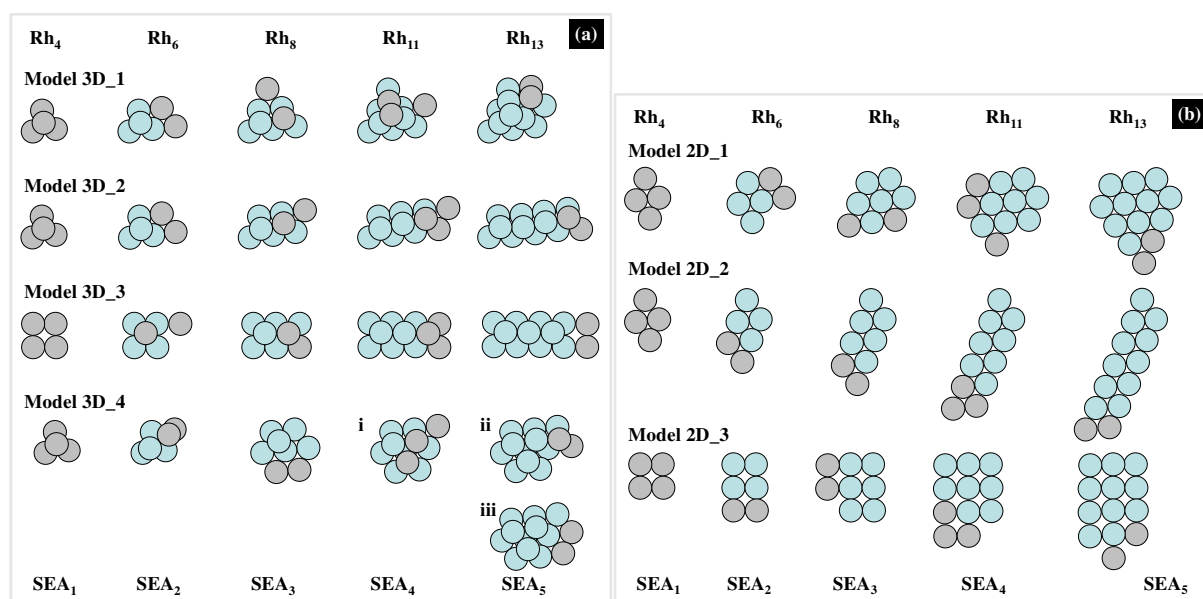


Figure 6. (a) 3D and (b) 2D Rh clusters (top view) proposed to be formed during the successive SEA processes. The Rh atoms added after each SEA process appear in grey, whereas those initially present in the preceding SEA step appear in light blue.

4.4.1. Comparison of the coordination numbers determined experimentally by EXAFS with those of the proposed Rh clusters, and adequacy of the proposed Rh clusters with the geometric constraints induced by the presence of oxotungstates on CeO₂

The calculated average coordination numbers (CN) of the Rh₄, Rh₆, Rh₈, Rh₁₁ and Rh₁₃ clusters of the various models shown in **Figure 6** are compared to those determined experimentally by EXAFS in **Table 4**. A first approach to estimate the reliability of the proposed model clusters consists in the calculation of the model deviation parameter (**Table 4**) referred to as the deviation of the average CN predicted by the corresponding model compared to the average CN determined experimentally by EXAFS. This deviation is expressed as the sum of the square difference between the average CN predicted by the corresponding clusters (**Figure 6**) and the average CN determined experimentally by EXAFS for each Rh/W(1.3)-SEA_i sample. Model 2D_3 shows the greatest deviation from the average CN determined experimentally by EXAFS, whereas the deviations of other models were found to be rather comparable, with Models 3D_2 and 3D_4 showing the lowest deviations. It must be recalled that the deposition of Rh in the present study was carried out on a tungstated-ceria support, which was found to exhibit mainly oxotungstate species by Raman (**Figure S1**), XP (**Table 2**) and X-ray Absorption (**Figure S2**) spectroscopies with a W surface density of 1.3 W/nm²_{CeO₂} (**Table 1**). The presence of tungstates brings about additional geometric constraints on the size of the Rh clusters. **Figure 7** shows (111)¹⁰⁰⁻¹⁰² and (100)¹⁰² CeO₂ surfaces nanostructured with oxotungstate species bonded to two atoms of the top oxygen surface layers and exhibiting a W

surface density of $1.3 \text{ W/nm}^2_{\text{CeO}_2}$. In these tungstated-CeO₂ surfaces, the area occupied by one isolated oxotungstate species was set to 0.16 nm^2 , as reported earlier by Boyse and Ko.¹⁰³ Among the proposed model clusters, **Figure 7a,c** shows that Rh₁₃ clusters of Models 3D_1, 3D_2, 3D_4 (cluster ii) and 3D_3 can be accommodated on the homogeneously tungstated surfaces from a steric point of view. Given that the (111) surface has been reported to be the most stable surface for CeO₂,¹⁰⁴ model 3D_3 may be ruled out. Regarding the 2D models on CeO₂(111) and CeO₂(100), **Figure 7b,c** shows that the Rh₁₃ clusters of Models 2D_1 and 2D_3 probably occupy too much space to be accommodated on the tungstated-ceria surfaces, whereas the accommodation of Rh₁₃ of Model 2D_2 seems to be possible.

Table 4. Comparison of the average coordination numbers (CN) of the proposed model Rh clusters shown in **Figure 6** (CN_{3D_i} and CN_{2D_i}) with those determined experimentally by EXAFS listed in **Table 3** (CN_{EXAFS}).

Samples	CN		CN deduced from the models						
	EXAFS		3D_1	3D_2	3D_3	3D_4	2D_1	2D_2	2D_3
Rh/W(1.3)-SEA ₁	3.8		3.0	3.0	2.0	3.0	2.5	2.5	2.0
Rh/W(1.3)-SEA ₂	3.7		3.3	3.3	3.0	4.0	3.0	3.0	2.3
Rh/W(1.3)-SEA ₃	4.2		4.0	4.0	4.0	4.0	3.5	3.3	2.5
Rh/W(1.3)-SEA ₄	3.9		4.7	4.4	4.4	4.7 ^b	3.8	3.5	2.7
Rh/W(1.3)-SEA ₅	4.0		5.2	4.6	4.2	4.9 ^c	4.0	3.5	2.8
<i>Model deviation^a</i>			2.9	1.5	4.1	2.1±0.1 ^d	2.7	3.4	11.0
<i>CN at infinite number of atoms</i>			12.0	5.3	5.3	9.0	6.0	4.0	4.0

^a the model deviation expresses the deviation of the CN predicted by the corresponding model compared to the CN determined experimentally by EXAFS. This deviation is expressed as the sum of the square difference between the CN predicted by the corresponding models (**Figure 6**) and the CN determined experimentally by EXAFS for each Rh/W(1.3)-SEA_i sample. A model deviation of 0 indicates full agreement between CN determined experimentally by EXAFS and predicted by the corresponding model clusters.

^b It must be noted that a Rh cluster with an atomicity of 11 Rh atoms has not been computed by Song et al.⁷⁸ and that cluster i shown in Model 3D_4 is proposed on the basis of the cluster with an atomicity of 10 reported by Song et al. to which 1 Rh atom was added.

^c Rh clusters with an atomicity of 13 have not been computed by Song et al.⁷⁸ either, and the clusters ii and iii shown in Model 3D_4 are proposed on the basis of the cluster with an atomicity of 10 reported by Song et al. to which 3 Rh atoms were added. The CN value listed in the Table for the 3D_4 model was estimated

from cluster ii (**Figure 6a**, Model 3D_4), whereas the choice of an alternative cluster with the same atomicity, i.e. 13 Rh atoms (**Figure 6a**, Model 3D_4, cluster iii) would have resulted in a CN of 4.8.

^d Average model deviation by considering the use of cluster ii and cluster iii in **Figure 6a** (Model 3D_4) and the corresponding CNs.

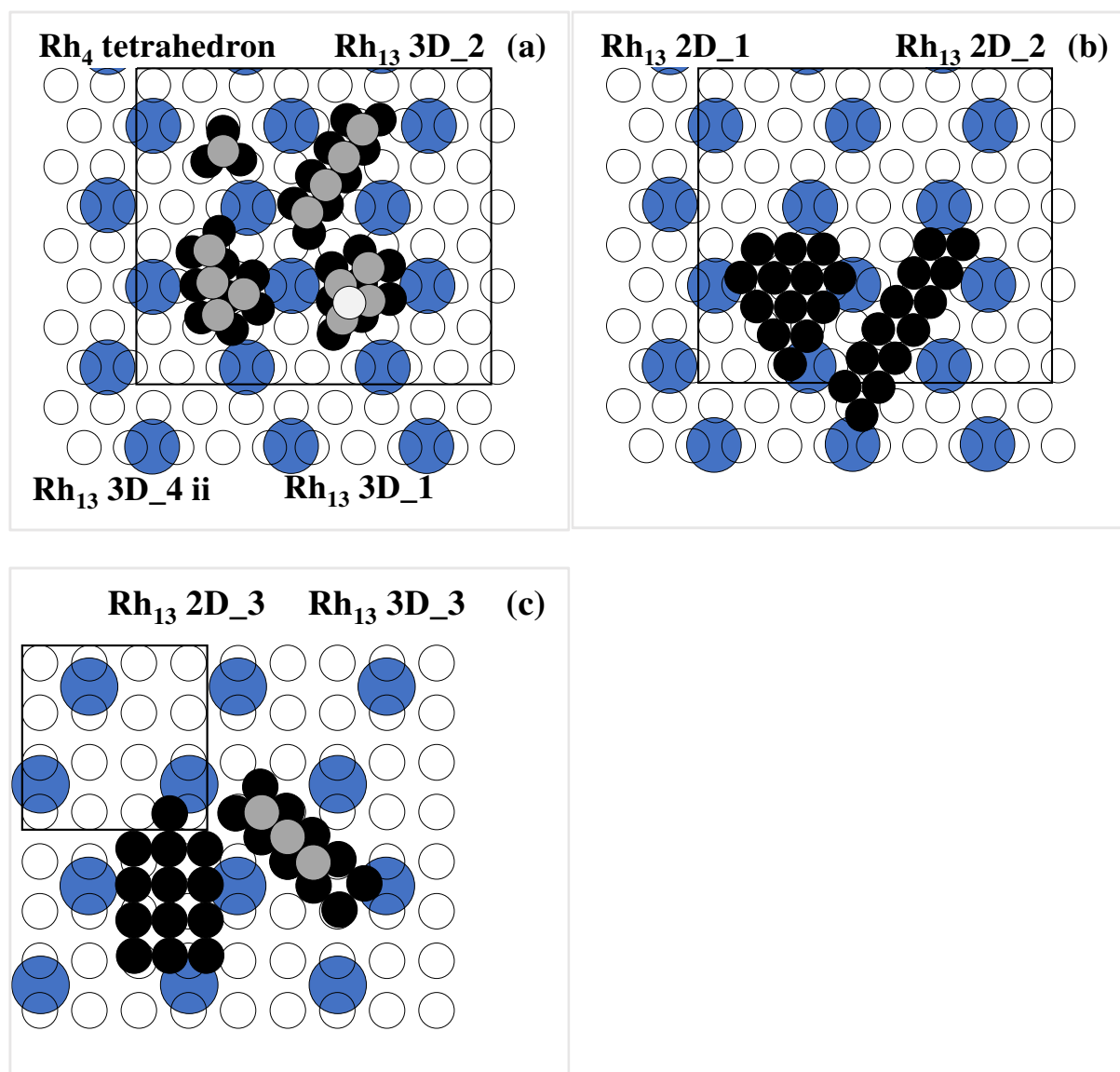


Figure 7. Schematic representation (top view) of Rh clusters on (a,b) (111) and (c) (100) tungstated-CeO₂ surfaces (W surface density of 1.3 W/nm²). ○ O²⁻, ● WO₄²⁻, ● Rh 1st layer, ● Rh 2nd layer, ● Rh 3rd layer. The rectangle and the square shown in (a,b) and (c) exhibit areas of 7.6 and 2.1 nm² for the (111) and (100) CeO₂ surfaces, respectively.

4.4.2. Reliability of the characterization of the Rh clusters by hydrogen chemisorption

The apparent discrepancy between the very low average CN (**Table 3**, indicative of very small Rh clusters) and the low H/Rh data (**Table 1**, indicative of large Rh particles) may indicate that the characterization of the Rh clusters of very low atomicity by the H₂ chemisorption technique does not provide a reliable description of the cluster sizes for the Rh/W(1.3)-SEA_i series, whereas a good agreement was found between H₂ chemisorption and EXAFS data for the larger Rh particles formed on the Rh_{NO3}/W(0.0)-CeO₂ sample (**Table 1**). The H/Rh experimental data may, nevertheless, be used together with the proposed atomicity of the Rh clusters to estimate the number of Rh atoms titrated by hydrogen in the Rh/W(1.3)-SEA_i series ($N_{\text{Rh H/Rh}}$, **Table 5**). These values are compared to the number of Rh atoms located in the 2nd and 3rd layers of the proposed clusters of Models 3D_1, 3D_2 and 3D_4 (**Table 5**), which are the 3D models determined as the most pertinent according to predicted average CN values and steric accommodation on the tungstated surfaces. Since the Rh atoms in the 1st layer of the proposed clusters are thought to be in close interaction with CeO₂, these Rh atoms were assumed to be less susceptible to chemisorb hydrogen and thus excluded as potential hydrogen chemisorption sites. **Table 5** shows that Model 3D_4 exhibits the highest deviation among the selected model clusters, which is essentially attributable to the poor correlation between the Rh atoms titrated by hydrogen and that identified for the Rh₈ cluster related to the Rh/W(1.3)-SEA₃ sample. Yet it must be recalled that geometry optimization of the Rh₈ cluster was performed on a clean CeO₂ (111) surface by Song et al.,⁷⁸ which differs substantially from the tungstated-CeO₂ surface studied in the present work. In contrast, the clusters proposed in Models 3D_1 and 3D_2 show a rather good agreement between the number of Rh atoms titrated by hydrogen and those present in the 2nd and 3rd layers of the proposed clusters (**Table 5**). It can be also noted that the correlation would be even better for the Rh/W(1.3)-SEA₂ sample in Models 3D_1



and 3D_2 by considering that the Rh₆ clusters would result from an equimolecular mixture of Rh₅ and Rh₇ clusters. In that eventuality, the average number of Rh atom present in the 2nd and 3rd layers (1.5) with that titrated by hydrogen (1.6) would be in excellent agreement (**Table 5**). Note also that considering this equimolecular mixture of Rh₅ and Rh₇ clusters for Rh/W(1.3)-SEA₂ would result in a predicted average CN (3.6) in closer agreement to that found experimentally by EXAFS (3.7, **Table 4**) compared to that listed in **Table 4** for Rh₆ clusters (3.3), and ultimately to slightly lower deviations than those listed in **Table 4** for both of these models. Although Model 2D_2 was found to be compatible with the tungstated CeO₂ (111) surface from a geometric viewpoint (**Figure 7b**) and showed only slightly higher deviation regarding the average CN compared to the 3D models of interest (**Table 4**), any correlation with the number of Rh titrated by hydrogen for this one layer-thick model clusters appears to be challenging as the Rh atoms in these 2D_2 model are found to be essentially equivalent (**Figure 6b**) and hydrogen atoms were computed to be coordinated to threefold adsorption sites on a Rh (111) surface.¹⁰⁵ Moreover, Rh clusters with a 3D-like morphology has been computed to be favored over the 2D morphology on a clean CeO₂ (111) surface.⁷⁸ Considering all of the above, it can be concluded that Models 3D_1 and 3D_2 appear as the most likely. In these models, the Rh subnanometric clusters must be at maximum two to three Rh layers thick and not larger than 5 Rh atoms. The influence of the presence of oxotungstates on CeO₂ on the morphology of the formed Rh clusters would certainly be of the greatest interest from a computational perspective and would probably also deserve to be a specific study in itself.

Table 5. Comparison of the number of Rh atoms in the 2nd and 3rd layers ($N_{\text{Rh } 3\text{D}_i}$) of the Rh clusters shown in **Figure 6a** (CN_{3D_i}) with those ($N_{\text{Rh H/Rh}}$) calculated from the proposed atomicity of the Rh clusters and the experimental H/Rh data listed in **Table 1**.

Samples	Rh clusters	H/Rh	$N_{\text{Rh H/Rh}}$	Number of Rh atoms		
				in the 2 nd and 3 rd layers of the Rh proposed model clusters		
				$N_{\text{Rh } 3\text{D}_1}$	$N_{\text{Rh } 3\text{D}_2}$	$N_{\text{Rh } 3\text{D}_4}$
Rh/W(1.3)-SEA ₁	Rh ₄	0.19	0.8	1.0	1.0	1.0
Rh/W(1.3)-SEA ₂	Rh ₆	0.27	1.6	1.0/1.5 ^b	1.0/1.5 ^b	2.0
Rh/W(1.3)-SEA ₃	Rh ₈	0.32	2.6	2.0	2.0	1.0
Rh/W(1.3)-SEA ₄	Rh ₁₁	0.33	3.6	4.0	3.0	3.0 ^c
Rh/W(1.3)-SEA ₅	Rh ₁₃	0.34	4.4	5.0	4.0	4.0/3.0 ^d
<i>Model deviation^a</i>				<i>1.2/0.9</i>	<i>1.3/1.0</i>	<i>3.2/5.0^e</i>

^a the model deviation expresses the deviation of the number Rh atoms present in the 2nd and 3rd layers of the clusters proposed in the corresponding models (**Figure 6a**) compared to the number Rh atoms calculated from the proposed atomicity of the Rh clusters and the experimental H/Rh data listed in **Table 1**. This deviation is expressed as the sum of the square difference between the number Rh atoms present in the 2nd and 3rd layers of the clusters proposed in corresponding models and the number Rh atoms calculated from the proposed atomicity of the Rh clusters and the experimental H/Rh for each Rh/W(1.3)-SEA_i sample. A model deviation of 0 indicates full agreement between the number of Rh atoms in the 2nd and 3rd layers of the proposed model clusters and those titrated by hydrogen.

^b The value of 1.5 reported in the Table for the Rh₆ cluster would result from an average value of Rh₅ (

) and Rh₇ () clusters in equimolar quantities where ● and ● represent Rh atoms in the 1st and the 2nd layer of the clusters, respectively.

^c It must be noted that a Rh cluster with an atomicity of 11 Rh atoms has not been computed by Song et al.⁷⁸ and that cluster i shown in Model 3D_4 is proposed on the basis of the cluster with an atomicity of 10 reported by Song et al. to which 1 Rh atom was added.

^d Rh clusters with an atomicity of 13 Rh atoms have not been computed by Song et al.⁷⁸ either, and the clusters ii and iii shown in Model 3D_4 are proposed on the basis of the cluster with an atomicity of 10 reported by Song et al. to which 3 Rh atoms were added. The number of Rh atoms listed in the Table for N_{Rh} 3D_4 were estimated from cluster ii/iii (**Figure 6a**, Model 3D_4).

^e Model deviation by considering the use of cluster ii/iii in **Figure 6a** (Model 3D_4).

4.4.3. Adequacy of the Rh clusters with N₂-FTIR spectra

N₂-FTIR shows that the intensity of the contribution at 2200 cm⁻¹ (assigned to the vibration of N₂ molecules chemisorbed on metallic rhodium (Rh⁰)⁷⁰) was found to increase as the number of successive SEA processes increased and seems to stabilize for Rh loadings higher than or equal to 0.56 wt% (Rh/W(1.3)-SEA₃, **Figure S6**). This trend is coherent with the trends observed regarding the H/Rh (**Table 1**) and normalized benzene hydrogenation rates (**Figure 4**, full circles). As N₂ was suggested to adsorb on low-coordinated Rh sites,¹⁰⁶ this study reveals that such sites were present in the Rh/W(1.3)-SEA_i series as well as on the 2.5 nm particles exhibited by the RhCl/W(0.0)-CeO₂ sample. A quantitative analysis on the intensity of this contribution on the lowly-loaded samples (from 0.23 to 0.56 wt% Rh, Rh/W(1.3)-CeO₂-SEA₁ to Rh/W(1.3)-CeO₂-SEA₃, **Figure S6**) remains challenging as it was computed that the intensity of the N₂-FTIR contribution was strongly dependent on the coordination of the Rh sites onto which N₂ adsorption occurred.¹⁰⁶ From a more qualitative point of view, the increase in resolution between the contributions at about 2200 and 2210 cm⁻¹ for the most highly-loaded sample (Rh/W(1.3)-SEA₅, **Figure S6a**) may be straightforwardly interpreted as the

development of 3D-structures comparable to those found in the 2.5 nm particles present in Rh_{Cl}/W(0.0)-CeO₂ (**Figure S6b**). As this increase in resolution between the two absorption peaks occurred exclusively for Rh/W(1.3)-SEA₅ (**Figure S6a**), and that Models 3D_1 and 3D_2 did not show obvious differences in terms of morphology between the Rh clusters with 11 and 13 Rh atoms (namely Rh₁₁ and Rh₁₃ clusters of Models 3D_1 and 3D_2 in **Figure 6a**), this may indicate a change in the morphology of Rh₁₃ compared to Rh₁₁ with a change from Rh₁₁ of Model 3D_2 to Rh₁₃ of Model 3D_1.

4.5. TEM imaging of the Rh clusters

Although it is very challenging to image Rh particles on CeO₂^{88, 107} due to a lack of contrast between the supported metal particles and the oxide support, several attempts were performed on the most highly-loaded Rh sample (Rh/W(1.3)-SEA₅, 0.88 wt% Rh) after ex situ reduction at 600 °C under H₂. However, after exposure to ambient air, it was not possible to detect the Rh particles, possibly due to reoxidation⁹⁷ and formation of 2D Rh oxides.⁷⁸ To overcome this limitation, Environmental TEM (ETEM) experiments were performed in which the samples were reduced in situ under low H₂ pressure at elevated temperatures. Rh particles (**Figure 8b**) could only be observed on one area of Rh_{Cl}/W(0.0)-CeO₂ (**Figure 8a**) after reduction at 600 °C under 5 mbar of H₂ within about 8 h of investigation. These particles were found to be slightly smaller (about 1.5 nm) than those expected from H₂ chemisorption data (2.5 nm). Under identical conditions, no Rh particles could be seen on Rh/W(1.3)-SEA₅. Few Rh clusters were, however, observed when the pressure of hydrogen was increased to 18 mbar at 600 °C (**Figure 8c**) and 650 °C (**Figure 8d**). These Rh clusters appeared to be subnanometric and seemed to confirm that the tungstated-CeO₂ support helped preserve smaller Rh clusters compared to the W-free CeO₂ support. The chemical composition of the region circled in white

in **Figure 8d** probed by Energy Dispersive X-ray Spectroscopy (EDS) analysis (0.74 ± 0.45 wt% Rh and 4.14 ± 0.45 wt% W) was found to be in reasonable agreement with that analyzed by XRF (0.88 wt% Rh and 3.00 wt% W).

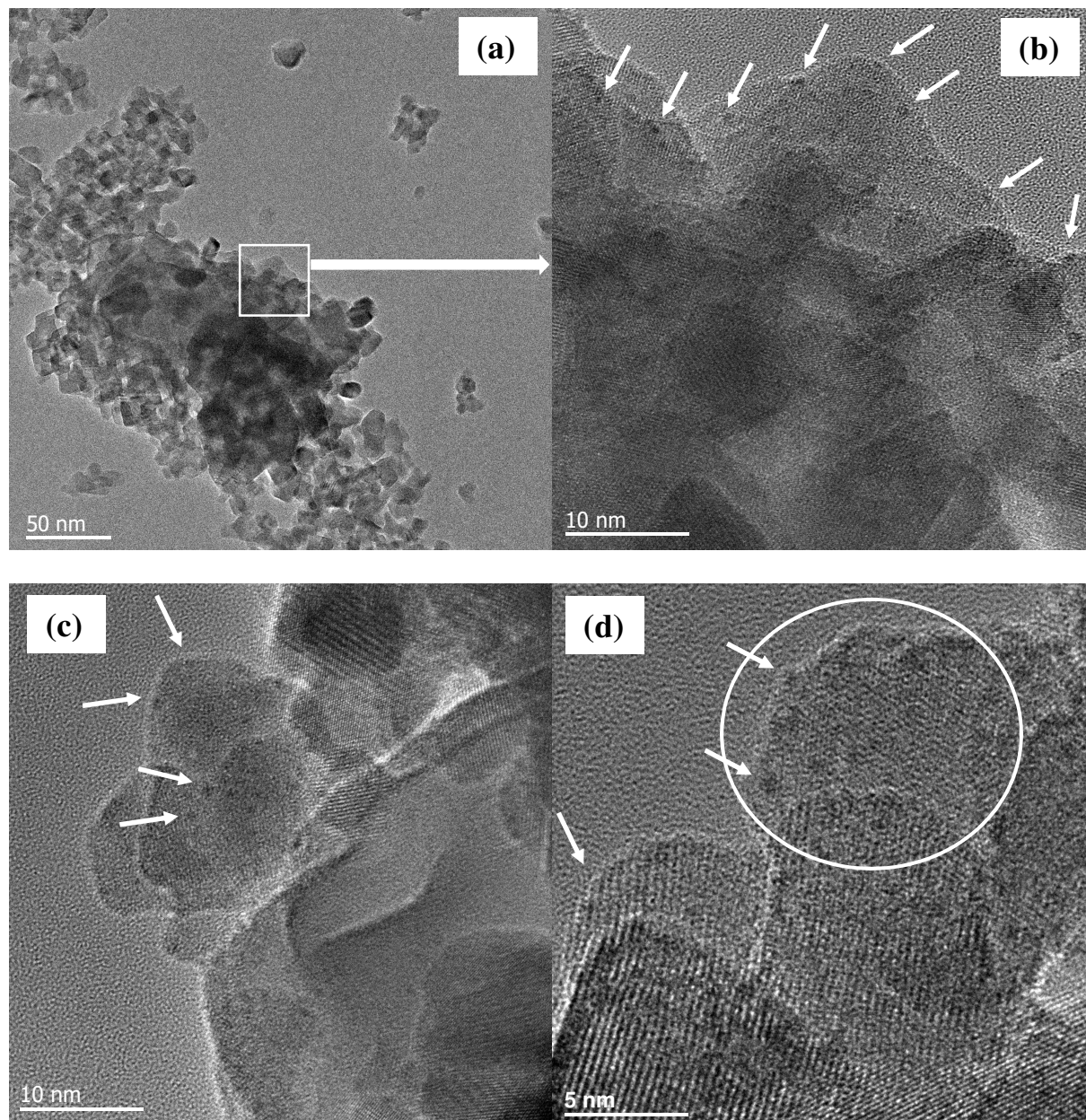


Figure 8. TEM images of (a) of $\text{RhCl}_3/\text{W}(0.0)\text{-CeO}_2$ recorded at $600\text{ }^\circ\text{C}$ and under 5 mbar of H_2 ((b) inset of (a)) and $\text{Rh}/\text{W}(1.3)\text{-CeO}_2$ recorded under (c) $600\text{ }^\circ\text{C}$ 18 mbar of H_2 and (d) ultra-high vacuum at RT after being exposed to 18 mbar of H_2 at $650\text{ }^\circ\text{C}$ in the ETEM facility. Some of the Rh particles are spotted with white arrows in (b) and (c) and the white circle in (c) displays the area for EDS analysis.

5. CONCLUSION

The present study demonstrates that the deposition of oxotungstates (with a W surface density of 1.3 W/nm^2) coupled with the selective deposition of Rh on the CeO_2 surface (via successive strong electrostatic adsorptions of an anionic $[\text{RhCl}_6]^{3-}$ precursor) significantly reduces Rh sintering after reduction at $600 \text{ }^\circ\text{C}$ under H_2 compared to a W-free CeO_2 support. The formation of the Rh oxidized clusters on the tungstated-ceria support was found to be occurring via a nucleation-growth process with a constant number of nucleation sites. Oxotungstates are found to decrease drastically the number of nucleation sites of CeO_2 and, therefore, to act as spacers leading to the isolation of the nucleation sites. Oxotungstates may also act as a physical barrier preventing the sintering of the Rh metallic phase in the course of the reduction step at high temperature. Various morphologies of subnanometric Rh clusters exhibiting a limited atomicity (4 to 13 Rh atoms) were considered and most were found to be consistent with the very low coordination numbers of 4.0 ± 0.2 determined experimentally by EXAFS. The proposed atomicities were also found to be coherent with those reported in earlier literature studies in which similarly low coordination numbers were obtained. Whereas hydrogen chemisorption appeared to be reliable to quantify the surface Rh atoms of 2.5 nm Rh particles supported on CeO_2 , this was not found to be the case for the characterization of the subnanometric clusters supported on the tungstated-ceria oxide. The Rh atoms titrated by hydrogen ranged from 19 to 34 %, while 100 % dispersion of the Rh metallic phase was suggested to be achieved for the subnanometric Rh clusters based on Rh average coordination numbers extracted from EXAFS data. Hydrogen chemisorption could, nevertheless, be used for the comparison of the subnanometric Rh clusters. The coordination numbers and the H_2 chemisorption data led the conclusion that the Rh subnanometric clusters must be at the maximum two to three Rh layers thick and not larger than 5 Rh atoms. The influence of the presence of oxotungstates on CeO_2 on the morphology of the formed subnanometric Rh clusters

would certainly be of the greatest interest from a computational perspective. Finally, the Rh weight-normalized benzene hydrogenation rates appeared to be lower on the subnanometric Rh clusters compared to the 2.5 nm Rh nanoparticles in agreement with the lower number of Rh atoms titrated by hydrogen on the former clusters. In contrast, the benzene hydrogenation turnover frequencies at 50 °C were found to be similar on the subnanometric Rh clusters and the 2.5 nm Rh nanoparticles ($0.12 \pm 0.3 \text{ s}^{-1}$), and in good agreement with earlier literature data reported on Rh supported on ceria-related oxides. The potential interest in these subnanometric Rh clusters for other catalytic reactions is currently being investigated.

Supporting Information

The supporting information is available free of charge at <https://pubs.acs.org/doi/xx.xxx/acs.jpcc.xxxxxxx>.

Raman spectra of the calcined $\text{W}(\text{W}/\text{nm}^2_{\text{CeO}_2})\text{-CeO}_2$ materials, Transmission X-ray absorption spectroscopy data of the W L_3 edge of Na_2WO_4 and reduced Rh/W(1.3)-SEA₅, NO_x uptakes of calcined $\text{W}(\text{W}/\text{nm}^2_{\text{CeO}_2})\text{-CeO}_2$ materials, Transmission X-ray absorption spectroscopy data of the Rh K edge of reduced Rh/W(1.3)-SEA_i and Rh_{NO3}/W(0.0)-CeO₂ samples, XP spectra in the Rh 3d region of Rh/W(1.3)-SEA_i and Rh_{Cl}/W(0.0)-CeO₂ after various pretreatments and N₂-FTIR spectra of reduced Rh(1.3)-SEA_i and Rh_{Cl}/W(0.0)-CeO₂.

Author Contributions

J.T.M. and N.M.S. carried out XANES and EXAFS measurements, and data analysis, and J.T.M. wrote the XAS sections. M.A. and P.V. performed ETEM imaging and EDS analysis on the catalyst samples. A.B. prepared the catalysts, carried out benzene hydrogenation

reaction, XRF, N₂ sorption and part of the NO_x-TPD experiments. J.B. supervised catalyst preparation and electrostatic adsorption capacity experiments. J.-M.K. performed Raman and N₂-FTIR experiments. C.M. performed XPS experiments and data analysis. C.S. supervised XRF and N₂ sorption experiments. F.S. and M.S. provided resources to and performed discussions about the project. C.T. conceptualized, supervised and initiated the research, performed H₂ chemisorption experiments and analysis, performed part of the NO_x-TPD experiments and analysis, performed analysis of the Raman, N₂-FTIR, benzene hydrogenation and XPS data, and wrote the manuscript. All authors read and commented on the manuscript.

ACKNOWLEDGMENTS

The authors thank Sorbonne Université and CNRS for providing funding (Crédits récurrents) and access to the analytical equipment used in the present study. ONERA (Office National d'Etudes et de Recherches Aéronautiques: The French Aerospace Lab) is acknowledged for providing additional funding to this work (Prestations de Service 2012-2014). The authors also thank the Institut des Matériaux de Paris Centre (IMPC, FR2482) and in particular S. Casale for the unsuccessful attempts in observing the Rh clusters over the Rh/W(1.3)-SEA₅ sample after ex situ reduction at 600 °C with a JEOL 2010 microscope operating at 200 kV. The Centre LYonnais de Microscopie (CLYM) is acknowledged for providing access to the FEI Titan ETEM. MRCAT operations are supported by the Department of Energy and the MRCAT member institutions. This research used resources of the Advanced Photon Source, a U.S. Department of Energy (DOE) Office of Science User Facility operated for the DOE Office of Science by Argonne National Laboratory under Contract No. DE-AC02-06CH11357.

REFERENCES

1. Munnik, P.; de Jongh, P. E.; de Jong, K. P., Recent Developments in the Synthesis of Supported Catalysts. *Chem. Rev.* **2015**, *115* (14), 6687-718.
2. Liu, L.; Corma, A., Metal Catalysts for Heterogeneous Catalysis: From Single Atoms to Nanoclusters and Nanoparticles. *Chem. Rev.* **2018**, *118* (10), 4981-5079.
3. Mehrabadi, B. A. T.; Eskandari, S.; Khan, U.; White, R. D.; Regalbuto, J. R., A Review of Preparation Methods for Supported Metal Catalysts. *Adv. Catal.* **2017**, *61*, 1-35.
4. Jones, J.; Xiong, H.; DeLaRiva, A. T.; Peterson, E. J.; Pham, H.; Challa, S. R.; Qi, G.; Oh, S.; Wiebenga, M. H.; Hernández, X. I. P., Thermally Stable Single-Atom Platinum-on-Ceria Catalysts via Atom Trapping. *Science* **2016**, *353* (6295), 150-154.
5. Thang, H. V.; Pacchioni, G.; DeRita, L.; Christopher, P., Nature of Stable Single Atom Pt Catalysts Dispersed on Anatase TiO₂. *J. Catal.* **2018**, *367*, 104-114.
6. Flytzani-Stephanopoulos, M.; Gates, B., Atomically Dispersed Supported Metal Catalysts. *Annu. Rev. Chem. Biomol. Eng.* **2012**, *3*, 545-574.
7. Therrien, A. J.; Hensley, A. J.; Marcinkowski, M. D.; Zhang, R.; Lucci, F. R.; Coughlin, B.; Schilling, A. C.; McEwen, J.-S.; Sykes, E. C. H., An Atomic-Scale View of Single-Site Pt Catalysis for Low-Temperature CO Oxidation. *Nature Catal.* **2018**, *1* (3), 192-198.
8. Pereira-Hernandez, X. I.; DeLaRiva, A.; Muravev, V.; Kunwar, D.; Xiong, H.; Sudduth, B.; Engelhard, M.; Kovarik, L.; Hensen, E. J. M.; Wang, Y.; Datye, A. K., Tuning Pt-CeO₂ Interactions by High-Temperature Vapor-Phase Synthesis for Improved Reducibility of Lattice Oxygen. *Nature Commun.* **2019**, *10* (1), 1358.
9. Kwak, J. H.; Hu, J.; Mei, D.; Yi, C.-W.; Kim, D. H.; Peden, C. H.; Allard, L. F.; Szanyi, J., Coordinatively Unsaturated Al³⁺ Centers as Binding Sites for Active Catalyst Phases of Platinum on γ -Al₂O₃. *Science* **2009**, *325* (5948), 1670-1673.
10. Qiao, B.; Wang, A.; Yang, X.; Allard, L. F.; Jiang, Z.; Cui, Y.; Liu, J.; Li, J.; Zhang, T., Single-Atom Catalysis of CO Oxidation Using Pt₁/FeO_x. *Nature Chem.* **2011**, *3* (8), 634-641.
11. Narula, C. K.; Allard, L. F.; Stocks, G. M.; Moses-DeBusk, M., Remarkable NO Oxidation on Single Supported Platinum Atoms. *Sci. Rep.* **2014**, *4* (1), 1-6.
12. Gawande, M. B.; Fornasiero, P.; Zbořil, R., Carbon-Based Single-Atom Catalysts for Advanced Applications. *ACS Catal.* **2020**, *10* (3), 2231-2259.
13. Duarte, R.; Safonova, O.; Krumeich, F.; van Bokhoven, J. A., Atomically Dispersed Rhodium on a Support: The Influence of a Metal Precursor and a Support. *Phys. Chem. Chem. Phys.* **2014**, *16* (48), 26553-26560.
14. Yang, X.-F.; Wang, A.; Qiao, B.; Li, J.; Liu, J.; Zhang, T., Single-Atom Catalysts: A New Frontier in Heterogeneous Catalysis. *Acc. Chem. Res.* **2013**, *46* (8), 1740-1748.
15. Van Hardeveld, R.; Hartog, F., The Statistic of Surface Atoms and Surface Sites on Metal Crystals. *Surf. Sci.* **1969**, *15*, 189-230.
16. Yates, D. J. C.; Murrell, L. L.; Prestridge, E. B., Ultradispersed Rhodium Rafts: Their Existence and Topology. *J. Catal.* **1979**, *57* (1), 41-63.

17. Blom, D. A.; Bradley, S. A.; Sinkler, W.; Allard, L. F., Observation of Pt Atoms, Clusters and Rafts on Oxide Supports, by Sub-Ångström Z-Contrast Imaging in an Aberration-Corrected STEM/TEM. *Microsc. Microanal.* **2006**, *12* (S02), 50-51.
18. Duncan, T.; Yates Jr, J.; Vaughan, R., A ¹³C NMR Study of the Adsorbed States of CO on Rh Dispersed on Al₂O₃. *J. Chem. Phys.* **1980**, *73* (2), 975-985.
19. Vaarkamp, M.; Miller, J. T.; Modica, F. S.; Koningsberger, D. C., On the Relation Between Particle Morphology, Structure of the Metal-Support Interface, and Catalytic Properties of Pt/γ-Al₂O₃. *J. Catal.* **1996**, *163* (2), 294-305.
20. Bergeret, G.; Gallezot, P., Particle Size and Dispersion Measurements. In *Handbook of Heterogeneous Catalysis*, G. Ertl, H. K., F. Schüth, J. Weitkamp, Ed. WILEY-VCH Verlag GmbH & Co. KGaA: Weinheim, 2008; Vol. 2, pp 738-765.
21. Burch, R., Knowledge and Know-How in Emission Control for Mobile Applications. *Catal. Rev.* **2004**, *46* (3-4), 271-334.
22. Montini, T.; Melchionna, M.; Monai, M.; Fornasiero, P., Fundamentals and Catalytic Applications of CeO₂-Based Materials. *Chem. Rev.* **2016**, *116* (10), 5987-6041.
23. Bernal, S.; Calvino, J.; Gatica, J.; Cartes, C. L.; Pintado, J., *Catalysis by Ceria and Related Materials*. 2nd ed.; Imperial College Press: London, 2002; Vol. 2, p 85-168.
24. Nagai, Y.; Dohmae, K.; Ikeda, Y.; Takagi, N.; Tanabe, T.; Hara, N.; Guilera, G.; Pascarelli, S.; Newton, M. A.; Kuno, O.; Jiang, H.; Shinjoh, H.; Matsumoto, S., In situ Redispersion of Platinum Autoexhaust Catalysts: An On-Line Approach to Increasing Catalyst Lifetimes? *Angew. Chem. Int. Ed. Engl.* **2008**, *47* (48), 9303-6.
25. Miller, J. T.; Schreier, M.; Kropf, A. J.; Regalbuto, J. R., A Fundamental Study of Platinum Tetraammine Impregnation of Silica: 2. The Effect of Method of Preparation, Loading, and Calcination Temperature on (Reduced) Particle Size. *J. Catal.* **2004**, *225* (1), 203-212.
26. Parks, G. A., The Isoelectric Points of Solid Oxides, Solid Hydroxides, and Aqueous Hydroxo Complex Systems. *Chem. Rev.* **1965**, *65* (2), 177-198.
27. Kosmulski, M., The pH Dependent Surface Charging and Points of Zero Charge. VIII. Update. *Adv. Colloid Interface Sci.* **2020**, *275*, 102064.
28. Noh, J. S.; Schwarz, J. A., Estimation of the Point of Zero Charge of Simple Oxides by Mass Titration. *J. Colloid Interface Sci.* **1989**, *130* (1), 157-164.
29. Feltes, T. E.; Espinosa-Alonso, L.; Smit, E. d.; D'Souza, L.; Meyer, R. J.; Weckhuysen, B. M.; Regalbuto, J. R., Selective Adsorption of Manganese Onto Cobalt for Optimized Mn/Co/TiO₂ Fischer-Tropsch Catalysts. *J. Catal.* **2010**, *270* (1), 95-102.
30. Samad, J. E.; Blanchard, J.; Sayag, C.; Louis, C.; Regalbuto, J. R., The Controlled Synthesis of Metal-Acid Bifunctional Catalysts: Selective Pt Deposition and Nanoparticle Synthesis on Amorphous Aluminosilicates. *J. Catal.* **2016**, *342*, 213-225.
31. Samad, J. E.; Blanchard, J.; Sayag, C.; Louis, C.; Regalbuto, J. R., The Controlled Synthesis of Metal-Acid Bifunctional Catalysts: The Effect of Metal: Acid Ratio and Metal-Acid Proximity in Pt silica-Alumina Catalysts for *n*-Heptane Isomerization. *J. Catal.* **2016**, *342*, 203-212.
32. Zecevic, J.; Vanbutsele, G.; De Jong, K. P.; Martens, J. A., Nanoscale Intimacy in Bifunctional Catalysts for Selective Conversion of Hydrocarbons. *Nature* **2015**, *528* (7581), 245-248.
33. Ben Moussa, O.; Tinat, L.; Jin, X.; Baaziz, W.; Durupthy, O.; Sayag, C.; Blanchard, J., Heteroaggregation and Selective Deposition for the Fine Design of Nanoarchitected Bifunctional Catalysts: Application to Hydroisomerization. *ACS Catal.* **2018**, *8* (7), 6071-6078.
34. Ro, I.; Xu, M.; Graham, G. W.; Pan, X.; Christopher, P., Synthesis of Heteroatom Rh-ReO_x Atomically Dispersed Species on Al₂O₃ and Their Tunable Catalytic Reactivity in Ethylene Hydroformylation. *ACS Catal.* **2019**, *9* (12), 10899-10912.

35. Bonnotte, T.; Doherty, R. P.; Sayag, C.; Krafft, J.-M.; Méthivier, C.; Sicard, M.; Ser, F.; Thomas, C., Insights into the WO_x Coverage-Dependent Location and Oxidation State of Noble Metals Supported on Tungstated Oxides: The Case of $\text{Rh}/\text{WO}_x\text{-Ce}_{0.62}\text{Zr}_{0.38}\text{O}_2$. *J. Phys. Chem. C* **2014**, *118* (14), 7386-7397.
36. Bernal, S.; Botana, F.; Calvino, J.; Cifredo, G.; Pe, J.; Pintado, J., HREM Study of the Behaviour of a Rh/CeO_2 Catalyst Under high Temperature Reducing and Oxidizing Conditions. *Catal. Today* **1995**, *23* (3), 219-250.
37. Bernal, S.; Calvino, J.; Cauqui, M.; Cifredo, G.; Jobacho, A.; Rodriguez-Izquierdo, J., Metal-Support Interaction Phenomena in Rhodium/Ceria and Rhodium/Titania Catalysts: Comparative Study by High-Resolution Transmission Electron Spectroscopy. *Appl. Catal. A: General* **1993**, *99* (1), 1-8.
38. Varga, E.; Pusztai, P.; Oszko, A.; Baan, K.; Erdohelyi, A.; Konya, Z.; Kiss, J., Stability and Temperature-Induced Agglomeration of Rh Nanoparticles Supported by CeO_2 . *Langmuir* **2016**, *32* (11), 2761-70.
39. Gatica, J. M.; Baker, R. T.; Fornasiero, P.; Bernal, S.; Blanco, G.; Kašpar, J., Rhodium Dispersion in a $\text{Rh}/\text{Ce}_{0.68}\text{Zr}_{0.32}\text{O}_2$ Catalyst Investigated by HRTEM and H_2 Chemisorption. *J. Phys. Chem. B* **2000**, *104* (19), 4667-4672.
40. Da Silva, A. M.; De Souza, K. R.; Jacobs, G.; Graham, U. M.; Davis, B. H.; Mattos, L. V.; Noronha, F. B., Steam and CO_2 Reforming of Ethanol Over Rh/CeO_2 Catalyst. *Appl. Catal. B: Environmental* **2011**, *102* (1-2), 94-109.
41. Cai, W.; Wang, F.; Van Veen, A.; Provendier, H.; Mirodatos, C.; Shen, W., Autothermal Reforming of Ethanol for Hydrogen Production Over an Rh/CeO_2 Catalyst. *Catal. Today* **2008**, *138* (3-4), 152-156.
42. Thormann, J.; Maier, L.; Pfeifer, P.; Kunz, U.; Deutschmann, O.; Schubert, K., Steam Reforming of Hexadecane Over a Rh/CeO_2 Catalyst in Microchannels: Experimental and Numerical Investigation. *Int. J. Hydrogen Energy* **2009**, *34* (12), 5108-5120.
43. Law, H. Y.; Blanchard, J.; Carrier, X.; Thomas, C., NO_x -TPD as a Tool to Estimate the Accessible Zirconia Surface of ZrO_2 -Containing Materials. *J. Phys. Chem. C* **2010**, *114* (21), 9731-9738.
44. Suhonen, S.; Valden, M.; Hietikko, M.; Laitinen, R.; Savimäki, A.; Härkönen, M., Effect of Ce-Zr Mixed Oxides on the Chemical State of Rh in Alumina Supported Automotive Exhaust Catalysts Studied by XPS and XRD. *Appl. Catal. A: General* **2001**, *218* (1-2), 151-160.
45. Xiaowei, L.; Mingmin, S.; Xi, H.; Haiyang, Z.; Fei, G.; Yan, K.; Lin, D.; Yi, C., Dispersion and Reduction of Copper Oxide Supported on WO_3 -Modified $\text{Ce}_{0.5}\text{Zr}_{0.5}\text{O}_2$ Solid Solution. *J. Chem. Phys. B* **2005**, *109* (9), 3949-3955.
46. Mamede, A.-S.; Payen, E.; Grange, P.; Poncelet, G.; Ion, A.; Alifanti, M.; Pârvulescu, V., Characterization of WO_x/CeO_2 Catalysts and Their Reactivity in the Isomerization of Hexane. *J. Catal.* **2004**, *223* (1), 1-12.
47. Scofield, J. H., Hartree-Slater Subshell Photoionization Cross-Sections at 1254 and 1487 eV. *J. Electron Spectrosc. Relat. Phenom.* **1976**, *8* (2), 129-137.
48. Thomas, C., Should W Surface Density of $\text{WO}_x\text{-ZrO}_2$ Catalysts Be Calculated With Respect To the Specific Surface Area of the Sample or That of ZrO_2 Only? *J. Phys. Chem. C* **2011**, *115* (5), 2253-2256.
49. Gorce, O.; Baudin, F.; Thomas, C.; Da Costa, P.; Djéga-Mariadassou, G., On the Role of Organic Nitrogen-Containing Species as Intermediates in the Hydrocarbon-Assisted SCR of NO_x . *Appl. Catal. B: Environmental* **2004**, *54* (2), 69-84.
50. Martinez-Arias, A.; Fernandez-Garcia, M.; Salamanca, L.; Valenzuela, R.; Conesa, J.; Soria, J., Structural and Redox Properties of Ceria in Alumina-Supported Ceria Catalyst Supports. *J. Phys. Chem. B* **2000**, *104* (17), 4038-4046.

51. Reddy, B. M.; Khan, A.; Lakshmanan, P.; Aouine, M.; Loridant, S.; Volta, J.-C., Structural Characterization of Nanosized CeO₂-SiO₂, CeO₂-TiO₂, and CeO₂-ZrO₂ Catalysts by XRD, Raman, and HREM Techniques. *J. Chem. Phys. B* **2005**, *109* (8), 3355-3363.
52. Sullivan, J. A.; Dulgheru, P.; Atribak, I.; Bueno-López, A.; García-García, A., Attempts at an In Situ Raman Study of Ceria/Zirconia Catalysts in PM Combustion. *Appl. Catal. B: Environmental* **2011**, *108*, 134-139.
53. Zdravković, J.; Simović, B.; Golubović, A.; Poleti, D.; Veljković, I.; Šćepanović, M.; Branković, G., Comparative Study of CeO₂ Nanopowders Obtained by the Hydrothermal Method from Various Precursors. *Ceram. Inter.* **2015**, *41* (2), 1970-1979.
54. Ma, Z.; Weng, D.; Wu, X.; Si, Z., Effects of WO_x Modification on the Activity, Adsorption and Redox Properties of CeO₂ Catalyst for NO_x Reduction With Ammonia. *J. Environ. Sci.* **2012**, *24* (7), 1305-1316.
55. Bigey, C.; Hilaire, L.; Maire, G., WO₃-CeO₂ and Pd/WO₃-CeO₂ as Potential Catalysts for Reforming Applications. *J. Catal.* **2001**, *198* (2), 208-222.
56. Salvati Jr, L.; Makovsky, L. E.; Stencel, J.; Brown, F.; Hercules, D. M., Surface Spectroscopic Study of Tungsten-Alumina Catalysts Using X-ray Photoelectron, Ion Scattering, and Raman Spectroscopies. *J. Phys. Chem.* **1981**, *85* (24), 3700-3707.
57. Dong, L.; Hu, Y.; Xu, F.; Lu, D.; Xu, B.; Hu, Z.; Chen, Y., A Study on the Surface Properties of Ceria-Supported Tungsten and Copper Oxides. *J. Phys. Chem. B* **2000**, *104* (1), 78-85.
58. Iwasaki, M.; Dohmae, K.; Nagai, Y.; Sudo, E.; Tanaka, T., Experimental Assessment of the Bifunctional NH₃-SCR Pathway and the Structural and Acid-Base Properties of WO₃ Dispersed on CeO₂ Catalysts. *J. Catal.* **2018**, *359*, 55-67.
59. Bertus, L. M.; Carcel, R. A., Prediction of TiO₂ and WO₃ Nanopowders Surface Charge by the Evaluation of Point of Zero Charge (PZC). *Environ. Eng. Manage. J.* **2011**, *10* (8), 1021-1026.
60. Wenderich, K.; Klaassen, A.; Siretanu, I.; Mugele, F.; Mul, G., Sorption-Determined Deposition of Platinum on Well-Defined Platelike WO₃. *Angew. Chem. Int. Ed.* **2014**, *53* (46), 12476-9.
61. Aleksandrov, A. V.; Gavrilova, N. N.; Nazarov, V. V., Colloid Chemical Properties of Hydrated Tungsten Trioxide Hydrosols. *Colloid J.* **2017**, *79* (3), 303-309.
62. Prabhu, S.; Manikumar, S.; Cindrella, L.; Kwon, O. J., Charge Transfer and Intrinsic Electronic Properties of rGO-WO₃ Nanostructures for Efficient Photoelectrochemical and Photocatalytic Applications. *Mater. Sci. Semicond. Process.* **2018**, *74*, 136-146.
63. Nabavi, M.; Spalla, O.; Cabane, B., Surface Chemistry of Nanometric Ceria Particles in Aqueous Dispersions. *J. Colloid Interface Sci.* **1993**, *160* (2), 459-471.
64. De Faria, L. A.; Trasatti, S., The Point of Zero Charge of CeO₂. *J. Colloid Interface Sci.* **1994**, *167* (2), 352-357.
65. Sun, J.; Zhang, J.; Fu, H.; Wan, H.; Wan, Y.; Qu, X.; Xu, Z.; Yin, D.; Zheng, S., Enhanced Catalytic Hydrogenation Reduction of Bromate on Pd Catalyst Supported on CeO₂ Modified SBA-15 Prepared by Strong Electrostatic Adsorption. *Appl. Catal. B: Environmental* **2018**, *229*, 32-40.
66. Gayen, A.; Priolkar, K.; Sarode, P.; Jayaram, V.; Hegde, M.; Subbanna, G.; Emura, S., Ce_{1-x}Rh_xO_{2-δ} Solid Solution Formation in Combustion-Synthesized Rh/CeO₂ Catalyst Studied by XRD, TEM, XPS, and EXAFS. *Chem. Mater.* **2004**, *16* (11), 2317-2328.
67. Wang, H.; Yates Jr, J. T., Infrared Spectroscopic Study of Molecular Nitrogen Chemisorption on Rhodium Surfaces. *J. Phys. Chem.* **1984**, *88* (5), 852-856.
68. Hadjiivanov, K. I.; Vayssilov, G. N., Characterization of Oxide Surfaces and Zeolites by Carbon Monoxide as an IR Probe Molecule. *Adv. Catal.* **2002**, *47*, 307-511.

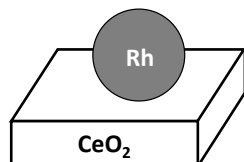
69. Binet, C.; Badri, A.; Lavalley, J.-C., A Spectroscopic Characterization of the Reduction of Ceria from Electronic Transitions of Intrinsic Point Defects. *J. Phys. Chem.* **1994**, *98* (25), 6392-6398.
70. Fontaine-Gautrelet, C.; Krafft, J.-M.; Djéga-Mariadassou, G.; Thomas, C., Evidence for Rh Electron-Deficient Atoms ($\text{Rh}^{\delta+}$) as the Catalytic Species for CO Oxidation when Supported on $\text{Ce}_{0.68}\text{Zr}_{0.32}\text{O}_2$: A Combined N_2 -FTIR, Benzene Hydrogenation, and Kinetic Study. *J. Catal.* **2007**, *247* (1), 34-42.
71. Fontaine-Gautrelet, C.; Krafft, J.-M.; Djéga-Mariadassou, G.; Thomas, C., On the Clarification of the IR Stretching Vibration Assignment of Adsorbed N_2 on Rh^0 and $\text{Rh}^{\delta+}$ Surface Atoms of Supported Rh Crystallites. *J. Phys. Chem. B* **2006**, *110* (20), 10075-10081.
72. Kozuch, S.; Martin, J. M., "Turning Over" Definitions in Catalytic Cycles. *ACS Catal.* **2012**, *2*, 2787-2794.
73. Job, N.; Lambert, S.; Chatenet, M.; Gommès, C. J.; Maillard, F.; Berthon-Fabry, S.; Regalbuto, J. R.; Pirard, J.-P., Preparation of Highly Loaded Pt/Carbon Xerogel Catalysts for Proton Exchange Membrane Fuel Cells by the Strong Electrostatic Adsorption Method. *Catal. Today* **2010**, *150* (1-2), 119-127.
74. Bueno-López, A.; Such-Basáñez, I.; Salinas-Martínez de Lecea, C., Stabilization of Active Rh_2O_3 Species for Catalytic Decomposition of N_2O on La-, Pr-Doped CeO_2 . *J. Catal.* **2006**, *244* (1), 102-112.
75. Zou, R.; Wen, S.; Zhang, L.; Liu, L.; Yue, D., Preparation of Rh-SiO₂ Fiber Catalyst With Superior Activity and Reusability by Electrospinning. *RSC Adv.* **2015**, *5* (121), 99884-99891.
76. Sheng, P.; Chiu, W.; Yee, A.; Morrison, S.; Idriss, H., Hydrogen Production from Ethanol Over Bimetallic Rh-M/CeO₂ (M=Pd or Pt). *Catal. Today* **2007**, *129* (3-4), 313-321.
77. Liu, J.; Tao, R.; Guo, Z.; Regalbuto, J. R.; Marshall, C. L.; Klie, R. F.; Miller, J. T.; Meyer, R. J., Selective Adsorption of Manganese onto Rhodium for Optimized Mn/Rh/SiO₂ Alcohol Synthesis Catalysts. *ChemCatChem* **2013**, *5* (12), 3665-3672.
78. Song, W.; Popa, C.; Jansen, A. P. J.; Hensen, E. J. M., Formation of a Rhodium Surface Oxide Film in $\text{Rh}_n/\text{CeO}_2(111)$ Relevant for Catalytic CO Oxidation: A Computational Study. *J. Phys. Chem. C* **2012**, *116* (43), 22904-22915.
79. Li, B.; Ezekoye, O. K.; Zhang, Q.; Chen, L.; Cui, P.; Graham, G.; Pan, X., Origin of Rh and Pd Agglomeration on the $\text{CeO}_2(111)$ Surface. *Phys. Rev. B* **2010**, *82* (12), 125422-1-125422-7.
80. Mittendorfer, F., Low-Dimensional Surface Oxides in the Oxidation of Rh Particles. *J. Phys. Cond. Matter* **2010**, *22* (39), 393001.
81. Van Delft, F. C. M. J. M.; Nieuwenhuys, B. E., Correlation of Nucleation- and Growth Mode With Wetting, Alloy Segregation, Catalyst Preparation and Strong-Metal Support Interaction. *Sol. State Ionics* **1985**, *16*, 233-240.
82. Tauster, S.; Fung, S.; Garten, R. L., Strong Metal-Support Interactions. Group 8 Noble Metals Supported on TiO₂. *J. Am. Chem. Soc.* **1978**, *100* (1), 170-175.
83. Haller, G. L.; Resasco, D. E., Metal-Support Interaction: Group VIII Metals and Reducible Oxides. *Adv. Catal.* **1989**, *36*, 173-235.
84. Barrault, J.; Alouche, A.; Paul-Boncour, V.; Hilaire, L.; Percheron-Guegan, A., Influence of the Support on the Catalytic Properties of Nickel/Ceria in Carbon Monoxide and Benzene Hydrogenation. *Appl. Catal.* **1989**, *46* (2), 269-279.
85. Binet, C.; Jadi, A.; Lavalley, J.-C.; Boutonnet-Kizling, M., Metal-Support Interaction in Pd/CeO₂ Catalysts: Fourier-Transform Infrared Studies of the Effects of the Reduction Temperature and Metal Loading. Part 1.—Catalysts Prepared by the Microemulsion Technique. *J. Chem. Soc. Faraday Trans.* **1992**, *88* (14), 2079-2084.

86. Cunningham, J.; O'Brien, S.; Sanz, J.; Rojo, J. M.; Soria, J. A.; Fierro, J. L. G., Exceptional Susceptibility of Ceria-Supported Rhodium Catalyst to Inhibitory SMSI Effects Including Acetone Hydrogenation. *J. Mol. Catal.* **1990**, *57* (3), 379-396.
87. Bernal, S.; Botana, F. J.; García, R.; Kang, Z.; López, M. L.; Pan, M.; Ramírez, F.; Rodríguez-Izquierdo, J. M., Characterisation of Rare Earth Oxide Supported Metal Catalysts. Study of Some Ceria Supported Rhodium Phases. *Catal. Today* **1988**, *2* (5), 653-662.
88. Bernal, S.; Botana, F.; Calvino, J.; Cauqui, M.; Cifredo, G.; Jobacho, A.; Pintado, J.; Rodríguez-Izquierdo, J., Microstructural and Chemical Properties of Ceria-Supported Rhodium Catalysts Reduced at 773 K. *J. Phys. Chem.* **1993**, *97* (16), 4118-4123.
89. Deleitenburg, C.; Trovarelli, A., Metal-Support Interactions in Rh/CeO₂, Rh/TiO₂, and Rh/Nb₂O₅ Catalysts as Inferred from CO₂ Methanation Activity. *J. Catal.* **1995**, *156* (1), 171-174.
90. Trovarelli, A.; Dolcetti, G.; de Leitenburg, C.; Kašpar, J.; Finetti, P.; Santoni, A., Rh-CeO₂ Interaction Induced by High-Temperature Reduction. Characterization and Catalytic Behaviour in Transient and Continuous Conditions. *J. Chem. Soc. Faraday Trans.* **1992**, *88* (9), 1311-1319.
91. Zhu Chen, J.; Talpade, A.; Canning, G. A.; Probus, P. R.; Ribeiro, F. H.; Datye, A. K.; Miller, J. T., Strong Metal-Support Interaction (SMSI) of Pt/CeO₂ and Its Effect on Propane Dehydrogenation. *Catal. Today* **2021**, *371*, 4-10.
92. Fajardie, F.; Tempère, J.-F.; Djéga-Mariadassou, G.; Blanchard, G., Benzene Hydrogenation as a Tool for the Determination of the Percentage of Metal Exposed on Low Loaded Ceria Supported Rhodium Catalysts. *J. Catal.* **1996**, *163*, 77-86.
93. Salin, L.; Potvin, C.; Tempere, J.-F.; Boudart, M.; Djéga-Mariadassou, G.; Bart, J.-M., Percentage of Metal Exposed on Commercial Three-Way Catalysts. *Ind. Eng. Chem. Res.* **1998**, *37* (12), 4531-4535.
94. Gatica, J. M.; Baker, R. T.; Fornasiero, P.; Bernal, S.; Kašpar, J., Characterization of the Metal Phase in NM/Ce_{0.68}Zr_{0.32}O₂ (NM: Pt and Pd) Catalysts by Hydrogen Chemisorption and HRTEM Microscopy: A Comparative Study. *J. Phys. Chem. B* **2001**, *105* (6), 1191-1199.
95. Force, C.; Belzunegui, J. P.; Sanz, J.; Martínez-Arias, A.; Soria, J., Influence of Precursor Salt on Metal Particle Formation in Rh/CeO₂ Catalysts. *J. Catal.* **2001**, *197* (1), 192-199.
96. Prestridge, E.; Yates, D., Imaging the Rhodium Atom With a Conventional High Resolution Electron Microscope. *Nature* **1971**, *234* (5328), 345-347.
97. van 't Blik, H. F. J.; van Zon, J. B. A. D.; Huizinga, T.; Vis, J. C.; Koningsberger, D. C.; Prins, R., Structure of Rhodium in an Ultradispersed Rh/Al₂O₃ Catalyst as Studied by EXAFS and Other Techniques. *J. Am. Chem. Soc.* **1985**, *107*, 3139-3147.
98. Jeong, H.; Lee, G.; Kim, B.-S.; Bae, J.; Han, J. W.; Lee, H., Fully Dispersed Rh Ensemble Catalyst to Enhance Low-Temperature Activity. *J. Am. Chem. Soc.* **2018**, *140* (30), 9558-9565.
99. Piotrowski, M. J.; Tereshchuk, P.; Da Silva, J. L. F., Theoretical Investigation of Small Transition-Metal Clusters Supported on the CeO₂(111) Surface. *J. Phys. Chem. C* **2014**, *118* (37), 21438-21446.
100. Namai, Y.; Fukui, K.-i.; Iwasawa, Y., Atom-Resolved Noncontact Atomic Force Microscopic Observations of CeO₂ (111) Surfaces with Different Oxidation States: Surface Structure and Behavior of Surface Oxygen Atoms. *J. Phys. Chem. B* **2003**, *107* (42), 11666-11673.
101. Gritschneider, S.; Reichling, M., Structural Elements of CeO₂ (111) Surfaces. *Nanotechnology* **2006**, *18* (4), 044024.

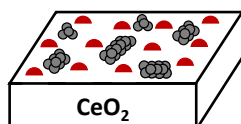
102. Mullins, D. R.; Albrecht, P. M.; Chen, T.-L.; Calaza, F. C.; Biegalski, M. D.; Christen, H. M.; Overbury, S. H., Water Dissociation on CeO₂ (100) and CeO₂ (111) Thin Films. *J. Phys. Chem. C* **2012**, *116* (36), 19419-19428.
103. Boyse, R. A.; Ko, E. I., Crystallization Behavior of Tungstate on Zirconia and Its Relationship to Acidic Properties. *J. Catal.* **1997**, *171* (1), 191-207.
104. Jiang, Y.; Adams, J. B.; Van Schilfgaarde, M., Density-Functional Calculation of CeO₂ Surfaces and Prediction of Effects of Oxygen Partial Pressure and Temperature on Stabilities. *J. Chem. Phys.* **2005**, *123* (6), 064701.
105. Löber, R.; Hennig, D., Interaction of Hydrogen With Transition Metal fcc (111) Surfaces. *Phys. Rev. B* **1997**, *55* (7), 4761.
106. Ligthart, D. A. J. M.; Filot, I. A. W.; Almutairi, A. A. H.; Hensen, E. J. M., Identification of Step-Edge Sites on Rh Nanoparticles for Facile CO Dissociation. *Catal. Commun.* **2016**, *77*, 5-8.
107. Ligthart, D. M.; van Santen, R. A.; Hensen, E. J., Supported Rhodium Oxide Nanoparticles as Highly Active CO Oxidation Catalysts. *Angew. Chem. Int. Ed.* **2011**, *123* (23), 5418-5422.

Table of Content Graphic

Strong Electrostatic Adsorption of $[\text{RhCl}_6]^{3-}$
on positively-charged CeO_2 / O_2 -400 °C / H_2 -600 °C



Rh nanoparticles (~2.5 nm)
on CeO_2



Rh clusters (< 1.0 nm)
on $\text{WO}_x(1.3 \text{ W/nm}^2)$ - CeO_2

Supporting Information

Successive Strong Electrostatic Adsorptions of $[\text{RhCl}_6]^{3-}$ on Tungstated-Ceria as an Original Approach to Preserve Rh Clusters From Sintering Under High-temperature Reduction

Jeffrey T. Miller,¹ Neil M. Schweitzer,² Mimoun Aouine,³ Philippe Vernoux,⁴ Abdelmalik Boufar,⁵ Juliette Blanchard,⁵ Jean-Marc Krafft,⁵ Christophe Méthivier,⁵ Céline Sayag,⁵ Frédéric Ser,⁶ Mickaël Sicard,⁶ Cyril Thomas^{5,*}

1- Purdue University, Davidson School of Chemical Engineering, 480 Stadium Mall Drive, West Lafayette, IN 47907-2100, USA

2- Department of Chemical and Biological Engineering, Northwestern University, Evanston, Illinois 60208-3113, USA

3- Univ Lyon, Université Claude Bernard Lyon 1, CNRS, Institut Lumière Matière, F-69622 Villeurbanne, France.

4- Univ Lyon, CNRS, Université Claude Bernard Lyon, IRCELYON, 2 Av. Albert Einstein, F-69626 Villeurbanne, France.

5- Sorbonne Université, CNRS, Laboratoire Réactivité de Surface, LRS, F-75005 Paris, France

6- Multi-Physics for Energetics Department, ONERA Université Paris Saclay, F-91123, Palaiseau, France.

* To whom correspondence should be addressed:

Dr. Cyril Thomas

Sorbonne Université, CNRS, Laboratoire Réactivité de Surface, LRS, UMR CNRS 7197, 4 Place Jussieu, Tour 43-53, 3^{ème} étage, Case 178, F-75252, Paris, France

e-mail: cyril.thomas@sorbonne-universite.fr

Tel: + 33 1 44 27 36 30

Fax: + 33 1 44 27 60 33

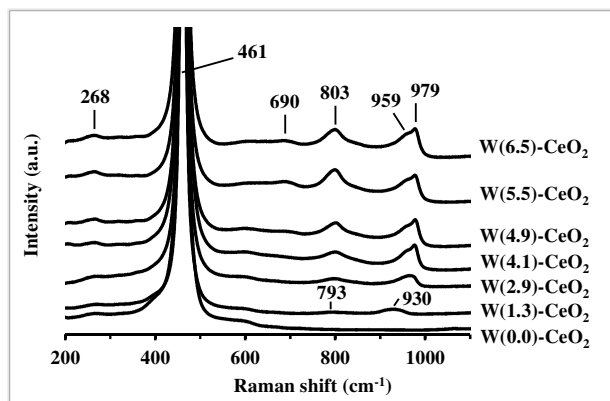


Figure S9. Raman spectra of the calcined W(W/nm²_{CeO₂})-CeO₂ materials.

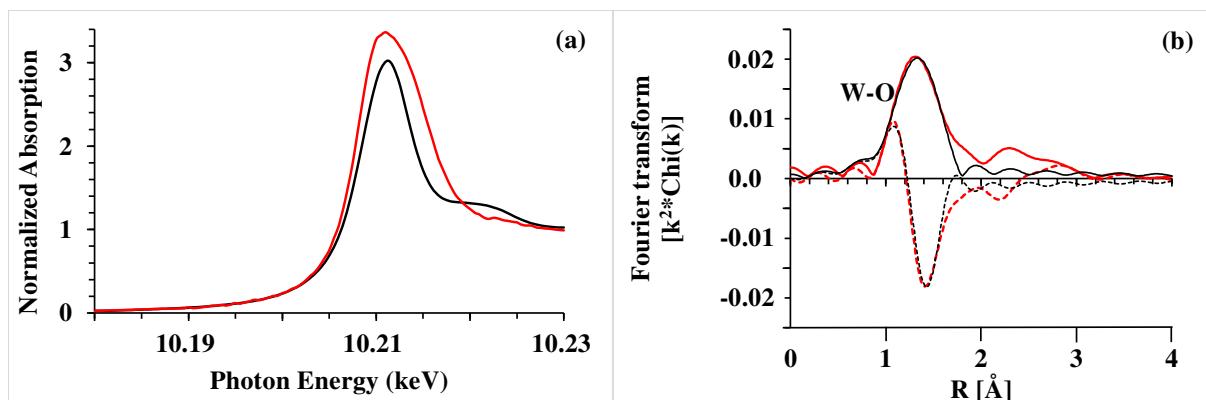


Figure S10. (a) W L₃-edge XANES spectra recorded from 10.18 to 10.23 keV of Na₂WO₄ (black) and Rh/W(1.3)-SEA₅ (red). (b) Fit (black lines) of the first shell W-O coordination of the magnitude (solid line) and imaginary parts (dotted line) of the k²-weighted Fourier transform ($\Delta k = 2.6\text{-}11.3 \text{ \AA}^{-1}$ and $\Delta R = 0.9\text{-}1.7 \text{ \AA}$) of the W L₃-edge EXAFS spectra (red lines). The spectrum of Rh/W(1.3)-SEA₅ was recorded at room temperature after reduction in flowing H₂ at 600 °C.

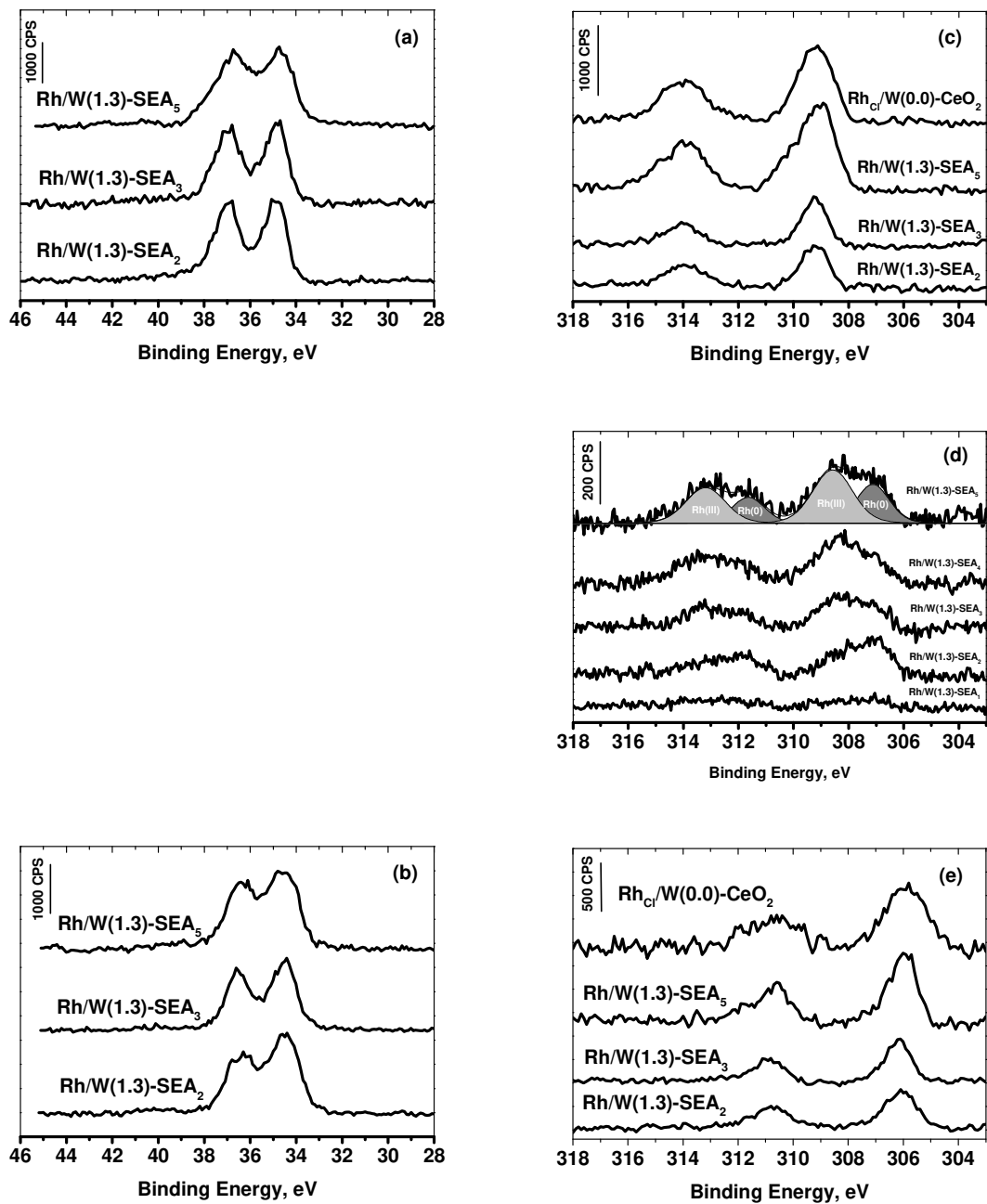


Figure S11. XPS spectra in the W 4f region after (a) ex-situ calcination under air at 400 °C for 2 h and exposure to ambient atmosphere and (b) in-situ XPS reduction under H₂ at 600 °C for 2 h, and in the Rh 3d region after (c) ex-situ calcination under air at 400 °C for 2 h and exposure to ambient atmosphere, (d) ex-situ reduction under H₂ at 600 °C for 2 h and exposure to ambient atmosphere and (e) in-situ XPS reduction under H₂ at 600 °C for 2 h

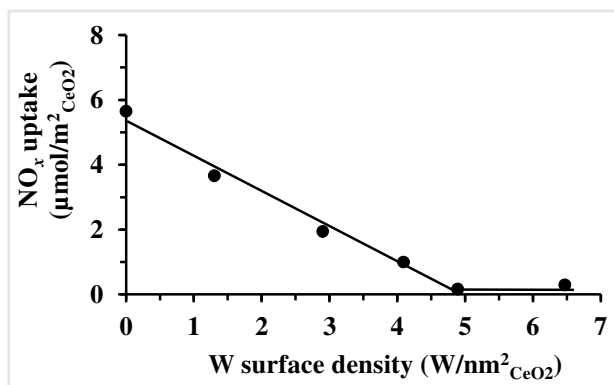


Figure S12. NO_x uptake as a function of the W surface density deduced from the NO_x-TPD profiles recorded on W(W/nm²)-CeO₂ materials ($0 \leq W/\text{nm}^2 \leq 6.5$) after exposure of 0.3 g of sample to 400 ppm NO_x and 8% O₂ in He (230 mL_{NTP}/min flow rate) at RT for about 4 h.

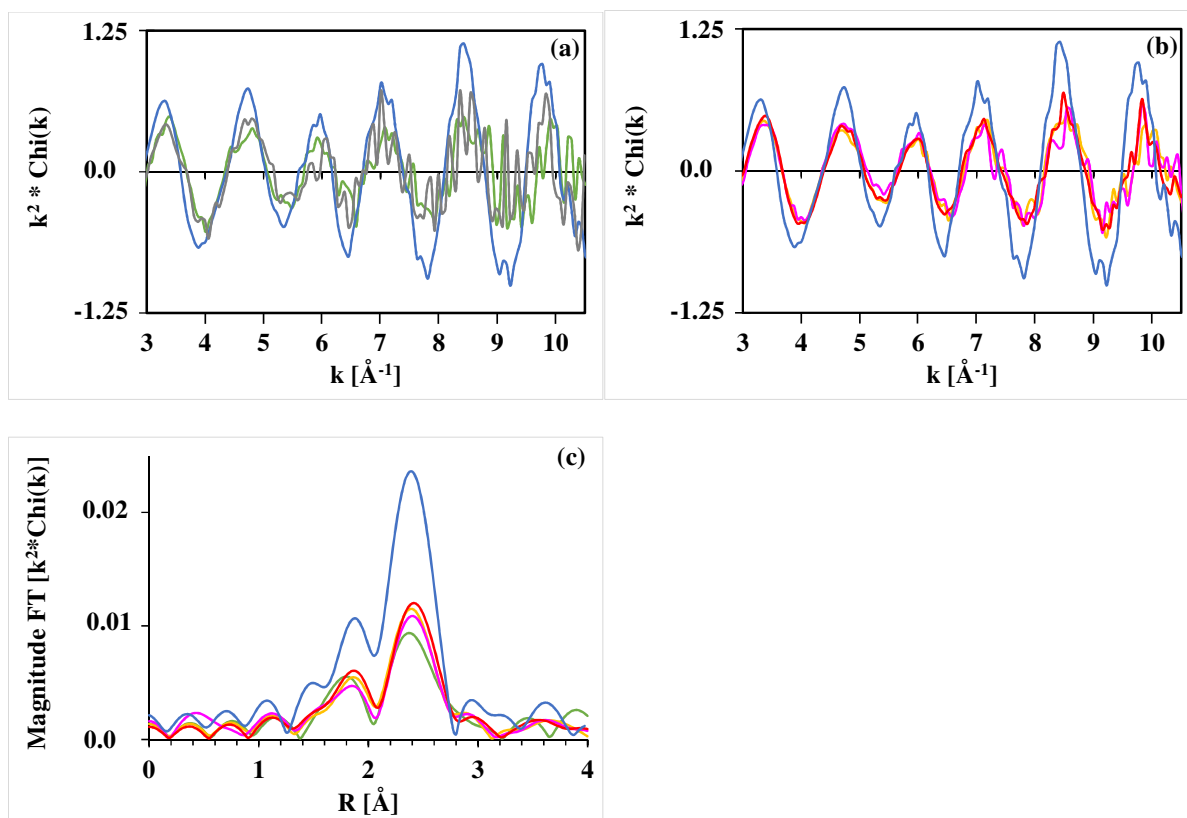


Figure S13. k^2 -weighted chi of the Rh K-edge EXAFS from 2.8-10.3 \AA^{-1} of (a) Rh/W(1.3)-SEA₁ (grey), Rh/W(1.3)-SEA₂ (green) and Rh_{NO₃}/W(0.0)-CeO₂ (blue), and (b) Rh/W(1.3)-SEA₃ (orange), Rh/W(1.3)-SEA₄ (purple), Rh/W(1.3)-SEA₅ (red) and Rh_{NO₃}/W(0.0)-CeO₂ (blue). (c) The magnitude of the k^2 -weighted Fourier transform of Rh K-edge EXAFS spectra ($\Delta k = 2.5-11.0 \text{ \AA}^{-1}$ and $\Delta R = 1.3-2.8 \text{ \AA}$) of Rh/W(1.3)-SEA₂ (green), Rh/W(1.3)-SEA₃ (orange), Rh/W(1.3)-SEA₄ (purple), Rh/W(1.3)-SEA₅ (red) and Rh_{NO₃}/W(0.0)-CeO₂ (blue). The spectra of the supported Rh samples were recorded at room temperature after reduction in flowing H₂ at 600 °C.

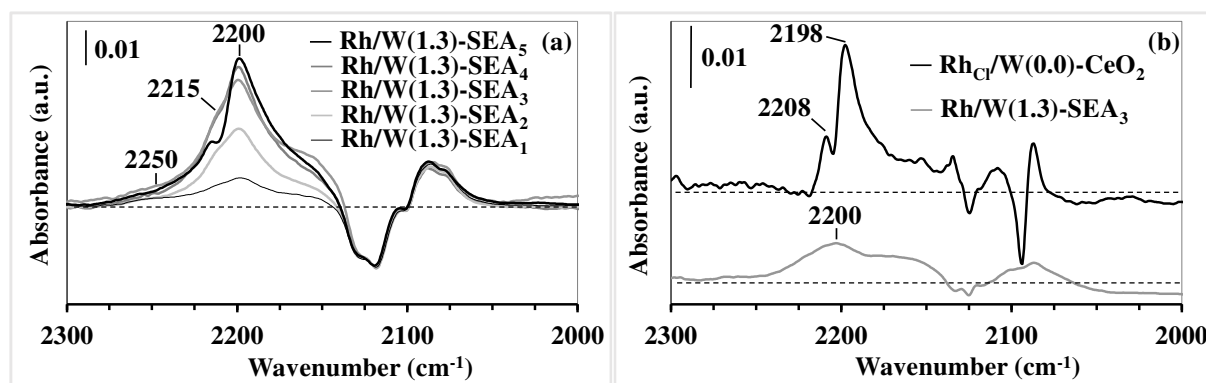


Figure S6. N₂-FTIR difference spectra of (a) the Rh/W(1.3)-SEA_i series and (b) Rh/W(1.3)-SEA₃ and RhCl/W(0.0)-CeO₂ after reduction at 600 °C for 2 h followed by evacuation (7.5×10^{-7} Torr) at 600 °C for 1 h and exposure to 10 Torr N₂ at -173 °C.